JGR Oceans

RESEARCH ARTICLE
10.1029/2020JC016085

Submesoscale Kinematic Properties in Summer and Winter Surface Flows in the Northern Gulf of Mexico

M. Berta[1], A. Griffa[1], A. C. Haza[2], J. Horstmann[3], H. S. Huntley[4], R. Ibrahim[5], B. Lund[2], T. M. Özgökmen[2], and A. C. Poje[5]

[1]CNR-ISMAR, La Spezia, Italy, [2]RSMAS, University of Miami, Coral Gables, FL, USA, [3]Helmholtz-Zentrum Geesthacht Centre for Materials and Coastal Research, Geesthacht, Germany, [4]School of Marine Science and Policy, University of Delaware, Newark, DE, USA, [5]Department of Mathematics, CSI-CUNY, New York, NY, USA

Key Points:
- Properties of submesoscale surface velocity gradients are compared in four distinct cases
- Differences between summer/winter launches are comparable with same-season spatial differences
- Signatures of submesoscale turbulence were found in three of four flows

Correspondence to:
A. C. Poje,
Andrew.Poje@csi.cuny.edu

Citation:
Berta, M., Griffa, A., Haza, A. C., Horstmann, J., Huntley, H. S., Ibrahim, R., et al. (2020). Submesoscale kinematic properties in summer and winter surface flows in the Northern Gulf of Mexico. *Journal of Geophysical Research: Oceans*, *125*, e2020JC016085. https://doi.org/10.1029/2020JC016085

Received 15 JAN 2020
Accepted 8 SEP 2020
Accepted article online 11 SEP 2020

Abstract Statistical properties of near-surface horizontal velocity gradients are obtained from four drifter experiments conducted in the Gulf of Mexico during Summer 2012 and Winter 2016. The data density provided by the near-simultaneous deployments of 90-326 surface drifters in each allows direct, drifter-based estimates of the scale dependence of velocity gradients at separation scales ranging from 200 m to 5 km. The robustness of these estimates, derived from uniquley sampled, nearly equilateral triplets, is confirmed by comparisons with estimates produced from larger drifter clusters, and with estimates based on concurrent Eulerian X-band radar observations. The winter launches were deployed above a ~80 m deep mixed layer, one in a region with nearly homogeneous horizontal density structure, the other in a region of strong surface density gradients associated with filaments of fresh Mississippi River water. The summer launches occurred in a shallow (10m) mixed layer, one launched across a mesoscale frontal jet separating regions of horizontally homogeneous density and the other, similar to the corresponding winter launch, also in a region filamented by shallow lenses of cold, fresh water. Seasonal differences are observed, with larger velocity fluctuations and greater variance in divergence and vorticity, especially at the smallest scales, in winter. Differences between same-season launches are, however, as large as seasonal differences. In both seasons, observations sampling regions directly impacted by fresh water fluxes show strongly skewed vorticity distributions, with cyclonic vorticity dominating strain. For the other launches, one in each season, strain dominated minimally skewed vorticity.

Plain Language Summary Variations in the near-surface currents act to redistribute floating material in the ocean. While much is known about variations at large scales, 50–100 km, the statistics of surface currents at smaller scales, 100m-10km, are not nearly as well documented. Here observations provided by hundreds of satellite-tracked drifting instruments (drifters) are used to measure such statistics in four distinct experiments, two each in summer and winter. The large number of drifters in each case allows us to determine, with a new level of statistical certainty, how surface current properties vary on scales ranging from 200 m to 5 km and provides benchmark observations of seasonal and spatial variability. Supporting observations of the upper-ocean density structure allows investigation of this impact on small-scale currents. Higher variability occurs in the more energetic winter flows, as expected. However, differences between two launches within a single season are equally large. Similarities between two flows, occurring in different seasons, can be traced to the presence of fresh, Mississippi River water in each. The drifter estimates were found to be consistent with measurements derived from a completely independent set of observations (surface radar images) indicating the potential for measuring near-surface current variations with large numbers of relatively inexpensive drifters.

1. Introduction

The structure and dynamics of the fluctuating near-surface ocean velocity field in the submesoscale wavelength band, 0.1–10 km, has been the focus of considerable research effort over the past several decades. As detailed in the reviews (Klein et al., 2019; McWilliams, 2016), submesoscale dynamics represent the transition regime between the mesoscales, accurately modeled by quasi-geostrophic theory, and the fully three-dimensional turbulence occurring at the microscale. Theoretically, this is an awkward regime where

the effects of stratification and planetary rotation are neither negligible nor dominant. Variability in submesoscale currents is associated with frontogenesis driven by horizontal density gradients and a variety of three-dimensional mixed layer instability mechanisms (Barkan et al., 2019; Boccaletti et al., 2007; Fox-Kemper et al., 2008; Hoskins, 1982; Mahadevan & Tandon, 2006; Thomas & Lee, 2005). Atmospheric momentum and buoyancy fluxes directly force the surface boundary layer, and the interaction of wind and waves provides an additional energy source via Langmuir turbulence at the lower range of the submesoscales (D'Asaro, 2014).

Energetic, ageostrophic submesoscale currents directly impact the oceanic transport and distribution of buoyant material (oil, plastics, biological and chemical tracers, etc.). Models and observations indicate that dispersion rates in the presence of submesoscale turbulence can readily exceed those produced by the geostrophic mesoscale alone by an order of magnitude (Haza et al., 2008; Poje et al., 2014). Equally important for the transport of surface trapped material is the distinction between horizontally divergence-free quasi-geostrophic turbulence and $\mathcal{O}(1)$ Rossby number submesoscale turbulence where surface convergence rates stronger than Coriolis, f, exist locally. Advection by submesoscale surface turbulence is highly anisotropic (Huntley et al., 2019), acting not only to spread, but also to trap tracers in surface convergence zones (D'Asaro et al., 2018).

Satellite chlorophyll and sea surface color images (Lévy et al., 2018; Shulman et al., 2015), as well as synthetic aperture radar images (Karimova & Gade, 2016; Munk et al., 2000), routinely show the strong filamentation produced by submesoscale currents. Direct, in situ observations, however, are less prevalent, as submesoscales are too large and evolve too rapidly to be easily mapped by single ship surveys (Özgökmen & Fischer, 2012). Consequently, much of what is known about the kinematic properties of near-surface submesoscale currents has been derived from simulations.

Modeling studies indicate that frontogenesis (Barkan et al., 2019; Capet et al., 2008a) and mixed layer instabilities (Boccaletti et al., 2007; Fox-Kemper et al., 2008) provide robust generation mechanisms for submesoscale currents. The resulting modeled flows, consistent with the linear instability associated with negative potential vorticity (Hoskins, 1982; Munk et al., 2000; Rudnick, 2001), suggest that submesoscale flows are characterized by highly cyclonic and convergent features with strongly positively skewed distributions of vertical vorticity and slightly negative skewed horizontal divergence. When model spatial resolution is fine enough to permit undamped motion at submesoscales, energetic submesoscale currents appear as ubiquitous model features in regions that are not dominated by larger mesoscale structures (Capet et al., 2008b). As noted by Barkan et al. (2017), this is particularly true in simulations of the Northern Gulf of Mexico where riverine fresh water fluxes provide a continuous supply of horizontal density gradients. Model results also confirm the expected seasonality in surface submesoscale energy (Mensa et al., 2013; Sasaki et al., 2014). The elevated potential energy associated with deeper mixed layers produces significantly stronger submesoscale flows in winter than summer, although strong seasonality may be modulated, at least in the Gulf Mexico, by fresh water fluxes (Luo et al., 2016).

The main goal of the present paper is to contribute to the relatively small number of direct, in situ, observations of the kinematic properties of the surface velocity field in the submesoscale range. In one of the earliest such studies, Shcherbina et al. (2013) used a unique data set provided by simultaneous acoustic Doppler current profiler (ADCP) measurements recorded from two ships in winter 2012, separated by 1 km, steaming 500 km south of the Gulf Stream to compute vertical vorticity, horizontal divergence, and strain at two depths. The results clearly showed enhanced variance of vorticity and divergence with highly positively skewed vorticity in the mixed layer, consistent with model results. Buckingham et al. (2016), using an array of moored ADCPs with separation distances ~1.5 km located in the North Atlantic, studied the seasonality of the vorticity distributions across the mixed layer and found significantly larger vorticity variance and skewness in winter. Ohlmann et al. (2017) investigated surface kinematic properties in the coastal Californian Current near Catalina Island using multiple, ~12-hr relaunches of 3×3 arrays of Lagrangian surface drifters with initial separation of 1 km. The results showed high sensitivity of submesoscale gradient statistics to launch location and time. Conditioning the launches based on the presence of fronts or eddies as determined from remote sea surface temperature imaging, the eddy launches were found to experience larger vorticity and significant positive divergence on average. The differences between the two types of flows, both observed during late winter-early spring, were larger than previously observed seasonality.

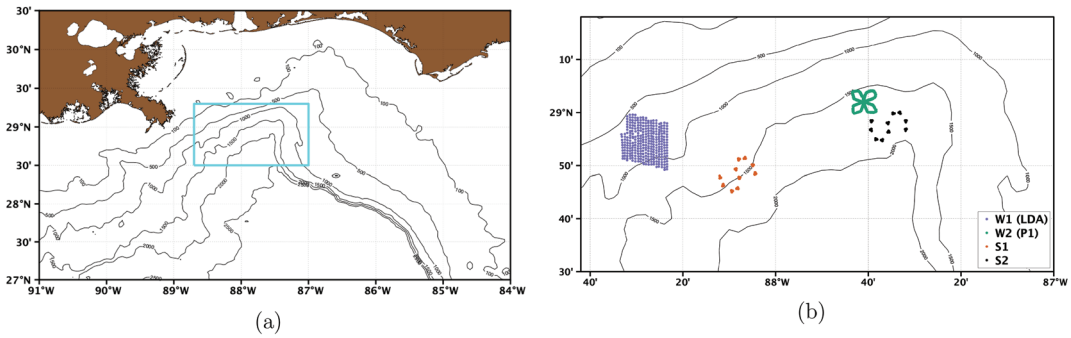

Figure 1. (a) Geographic location of the four drifter deployments in the Northern Gulf of Mexico and (b) the deployment patterns used in each experiment. LASER deployments, winter 2016: W1 (purple), W2 (green). GLAD deployments, summer 2012: S1 (red), S2 (black).

In this paper, we investigate surface kinematic properties in the submesoscales using data provided by four large, quasi-synoptic surface drifter deployments in the DeSoto Canyon region of the Gulf of Mexico. Each launch consisted of 90–326 drifters and was conducted within a 4–14 hr window. The data sets were collected during the Grand LAgrangian Deployment (GLAD) in the summer of 2012 and the LAgrangian Submesoscale ExpeRiment (LASER) conducted during the winter of 2016. The four launch locations provide a means of assessing the degree of spatial inhomogeneity (see Figure 1), seasonality and, with concurrent hydrographic observations at each launch, the role of local buoyancy gradients in determining the statistics of submesoscale surface velocity gradients. In addition, the high drifter data density permits analysis of the scale dependence of the standard signatures of submesoscale turbulence for separation distances ranging from hundreds of meters to several kilometers. The results aid in determining the variability in localized observations of submesoscale turbulence statistics.

Drifter triplets are used to investigate horizontal vorticity ζ and divergence δ in terms of probability density functions, means, variances, and skewness across the scales. Uncertainties in the gradient estimates arising from the Lagrangian nature of the measurements are considered. It is well established that drifter triplets tend to elongate (Berta et al., 2016; LaCasce & Ohlmann, 2003); the resulting high aspect ratios are the main source of errors in the kinematic property estimates. Drifters also tend to oversample convergent regions, leading to biases in the statistics. To minimize these problems, we resample the triplets every hour, selecting only quasi-equilateral configurations formed by unique drifter trajectories, and we consider only the first 1–4 days after deployment. Each flow realization is therefore captured quasi-synoptically and characterized using the environmental data collected at launch. As additional validation, we compare the kinematic property estimates from drifter triplets with alternative estimates from larger drifter clusters, as well as with Eulerian estimates from X-band radar surface current data. An analysis of the scale dependence of velocity differentials based on drifter pairs shows broad consistency with the triplet-based investigation.

Data sources and methods used in the analysis are introduced in section 2, while the general environmental characteristics are described in section 3. Results are presented in section 4. Section 5 provides a summary and conclusions.

2. Materials and Methods

2.1. Launch Location and Configuration of the Four Experiments

All four drifter launches were performed in the northern Gulf of Mexico on the northwestern side of the DeSoto Canyon, to the east of the Mississippi River delta (Figure 1a). Different deployment patterns were used, but each covered a roughly square area with sidelengths ~10–20 km (Figure 1b).

The summer GLAD deployments S1 (west) and S2 (east) (Berta et al., 2016; Poje et al., 2014) were launched in less than 5 hr each on 22 and 26 July 2012, respectively. Each consisted of 90 drifters arranged in nested equilateral triangles in 10 nodes in an "S" shape (red and black in Figure 1b). The design sidelengths of the triangles were 100 and 500 m, and the nodes were spaced 2–4 km apart. The first winter LASER deployment, W2 (east), (green in Figure 1b) was designed as a clover shape, with each node composed of an isosceles right triangle with legs of length 250 m. A total of 309 drifters were launched over ~5 hr, starting on 21 January

2016 at 13:25 UTC. The other winter deployment, W1 (west), (purple in Figure 1b) was aimed to create a regular 18×18 grid with $\Delta x \approx 1$ km. A total of 326 drifters were launched over 14 hr starting on 7 February 2016 at 02:05 UTC. All drifter deployments provided original pairs and triplets with distances in the range of several hundred meters to a few km. Each of the summer launches can be paired with a winter launch that samples a similar geographic area (Figure 1b): Summertime S1 (west) and wintertime W1 (west) are located on the west side of the DeSoto Canyon close to the Mississippi River outflow, while summertime S2 (east) and wintertime W2 (east) are located to the east, further from the Mississippi River outflow.

Hydrographic observations were collected during all drifter launches. In the summer experiment, conductivity-temperature-density (CTD) casts were taken at one or two locations in each of the 10 drifter nodes of each deployment. Much more extensive data was obtained during the subsequent winter experiment. Prior to and during each winter launch, the R/V *Walton Smith* performed multiple transects of the launch region deploying a Moving Vessel Profiler (MVP) to obtain CTD data down to depths below 200 m with horizontal resolution $\leq$ km depending on ship speed. Additionally, estimates of near-surface current velocities were obtained from backscatter images from a ship-mounted, coherent-on-receive marine X-band (9.4 GHz) radar (Lund et al., 2018).

2.2. Near-Surface, GPS-Tracked Drifters

Drifters deployed during the summer experiment were based on the Coastal Ocean Dynamics Experiment (CODE) design of Davis (1985). Four "wings," 1 m long and 0.5 m wide, were attached at right angles to a plastic pipe, with a compartment for the electronics at the top and buoys at the end of each wing. These types of drifters have been shown to follow the currents of the top 1 m of the water column with minimal windage (Davis, 1985).

For the much larger winter deployments, an almost entirely biodegradable drifter was developed, now known as the CARTHE (Consortium for the Advanced Research on Transport of Hydrocarbon in the Environment) drifter (Novelli et al., 2017). It consists of a donut-shaped float with a central compartment for the electronics, tethered to a drogue extending to 60 cm below the surface. In the early design used in this experiment, a rubber tube connected the two pieces. This proved unreliable, however, (and has since been replaced with a short chain): During strong wind and wave events, quite a few drifters lost their drogues. Fortunately, it was possible to identify drogue-loss from the differential motion of drogued and undrogued drifters (Haza et al., 2018). For our purposes here, we use only data from drogued drifters. Extensive testing, both in a wave tank and at sea, confirmed that the motion of drogued CARTHE drifters represents the integrated effect of the top 60 cm of the water column (Novelli et al., 2017). Due to the flexible connector between float and drogue, the drifter is minimally affected by wave rectification.

Both types of drifters were equipped with SPOT GPS units to report positions in real time, nominally every 5 min with a nominal accuracy of 7 m. The raw trajectory data was processed to remove outliers, then low-pass filtered with a 1-hr cut-off, and interpolated to uniform 15-min intervals, following the procedure of Yaremchuk and Coelho (2015).

2.3. Near-Surface Hydrographic Surveys

During the winter drifter deployments, along-track profiles of temperature and salinity were measured from the R/V *Walton Smith* from depths of ~200 m to within a few meters of the surface using a moving vessel profiler (MVP-300) manufactured by ODIM Brooke Ocean/Rolls-Royce (Klymak et al., 2016). Raw CTD observations from the profiler were converted to salinity and potential density and gridded on 1 m vertical bins with horizontal resolution ~1.4 km for the lead-up to the W2 (east) launch and ~900 m during each radiator leg of the W1 (west) launch.

2.4. X-Band Radar Surface Velocity Estimates

As part of the winter experiment, backscatter images were collected every 2 s from a Doppler marine X-band (9.4 GHz) radar within a range of 3.2 km of the vessel (see for details of the setup Lund et al., 2018). They were corrected for ship motion and georeferenced, before partitioning into evenly distributed and partially overlapping circular analysis windows covering ~0.7 km^2 and 30 min time windows. Near-surface currents were derived from the difference between the radar observed long (>15 m) surface waves phase velocity and that given by the linear dispersion relation of gravity waves (Huang et al., 2016; Senet et al., 2001). Therefore,

the effective current depth depends on the lengths of the underlying surface waves (Lund et al., 2018) and is estimated here to be ~1–5 m, somewhat deeper than the drifter depth. The processed product is a series of maps of the surface velocity field in a roughly 10×10 km region on a grid with horizontal resolution $\Delta x = 480$ m, representing an average over a 30-min window.

2.5. Estimates of Kinematic Properties From Drifter Triplets

2.5.1. Methodology

A variety of methods exists to estimate kinematic properties from groups of drifter trajectories. They fall into three broad categories: (1) least squares fits to Taylor expansions around either a centroid position (e.g., Okubo et al., 1976) or a centroid velocity (e.g., Method I of Molinari & Kirwan 1975) for a cluster of drifters; (2) area-averaged estimates from the convex hull of a cluster of drifters (e.g., Method II of Kawai, 1985a; Molinari & Kirwan 1975); (3) gradients computed from interpolated velocity fields (e.g., Gonçalves et al., 2019).

A minimum of three drifters is required by all these algorithms. (A method to estimate kinematic properties from single trajectories was proposed by Kirwan (1988) but has not been substantially validated.) To maximize the number of nonoverlapping realizations, especially at the small scales, we thus use drifter triplets. For each triplet, we estimate vorticity ζ, divergence δ, and shear and normal deformation, each averaged over the area defined by the three vertices. Shear and normal deformation are combined to calculate the strain rate α, defined by

$$\alpha^2 := \left(\overline{u_x - v_y}\right)^2 + \left(\overline{u_y + v_x}\right)^2, \tag{1}$$

where the overbar indicates an area average.

We follow Kawai (1985a) to derive these spatially averaged kinematic property estimates from Green's Theorem, which relates the area average of the curl of a vector-valued function $\mathbf{F}_\kappa$ to the line integral of $\mathbf{F}_\kappa$ along the boundary of the area:

$$\frac{1}{A}\iint \nabla \times \mathbf{F}_\kappa \, \mathrm{d}A = \frac{1}{A}\oint \mathbf{F}_\kappa \cdot \mathrm{d}\mathbf{s}, \tag{2}$$

(where A denotes the triangle area). Setting $\mathbf{F}_\zeta = \mathbf{u} = (u, v)$ gives the average vorticity via the standard circulation theorem:

$$\overline{\zeta} := \frac{1}{A}\iint \nabla \times \mathbf{u} \, \mathrm{d}A = \frac{1}{A}\oint \mathbf{u} \cdot \mathrm{d}\mathbf{s}. \tag{3}$$

The average vorticity measures the rotational component of the flow. The average divergence, which captures spreading (or accumulating) characteristics of the flow, can be estimated by setting $\mathbf{F}_\delta = (-v, u)$:

$$\overline{\delta} := \frac{1}{A}\iint \left(u_x + v_y\right) \, \mathrm{d}A = \frac{1}{A}\oint (-v, u) \cdot \mathrm{d}\mathbf{s}. \tag{4}$$

With $\mathbf{F}_{\alpha_S} = (-u, v)$ and $\mathbf{F}_{\alpha_N} = (v, u)$, the strain rate, combining shear and normal terms, can be estimated using:

$$\overline{\alpha}^2 := \left(\overline{u_x - v_y}\right)^2 + \left(\overline{u_y + v_x}\right)^2 = \left[\frac{1}{A}\oint (-u, v) \cdot \mathrm{d}\mathbf{s}\right]^2 + \left[\frac{1}{A}\oint (v, u) \cdot \mathrm{d}\mathbf{s}\right]^2 \tag{5}$$

The strain rate reflects area-preserving deformation.

Velocities at each drifter position are estimated from the spline coefficients used for the interpolation onto even time intervals. Line integrals are computed assuming a linear change in velocity along each edge segment.

All methods are subject to errors and uncertainties deriving from approximations in the algorithms and computations, as well as from GPS position errors. Monte Carlo simulations show that GPS position errors are generally negligible except for nearly aligned triads. In fact, the tendency of drifter clusters to evolve, under the effects of strain, toward high aspect ratio configurations is a major source for errors more generally (Berta et al., 2016; Essink, 2019; Ohlmann et al., 2017). In the limit of collinear configurations, kinematic property estimation becomes impossible.

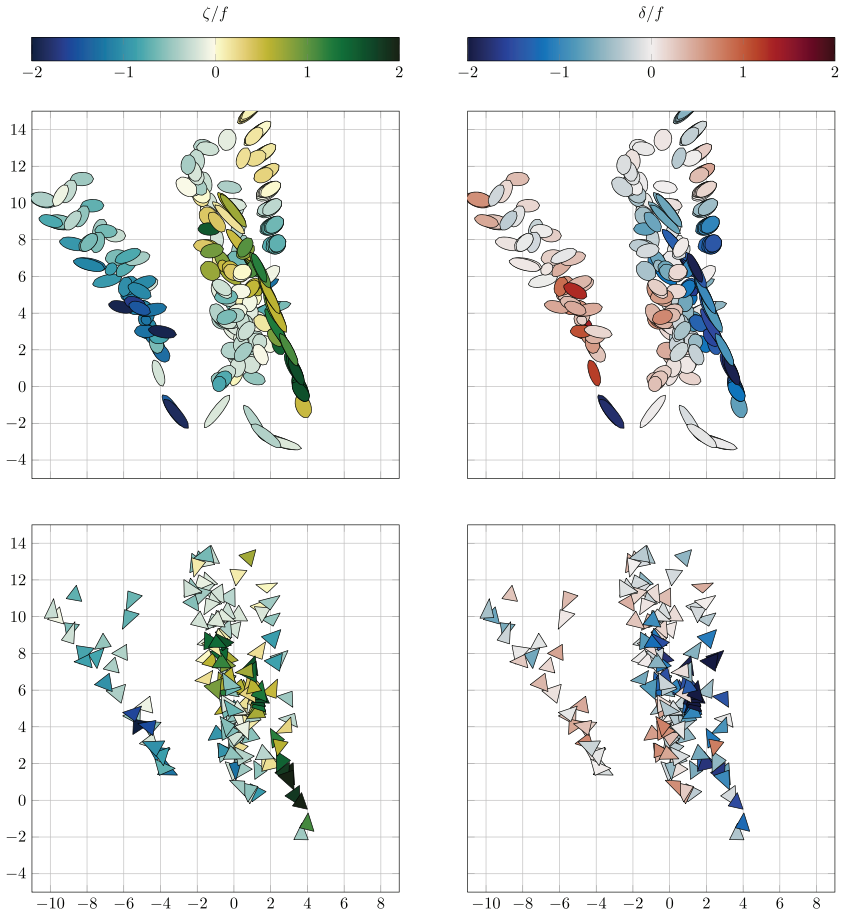

Figure 2. Comparison of vorticity (left) and divergence (right) estimates derived from drifter clusters (top) and drifter triplets (bottom) for the winter W2 (east) launch. Data from all available 1-hr averaged nearly equilateral triplets and clusters with $N > 5$ and aspect ratio <5 for the first 12 hr after the last drifter launch are shown. The nominal length-scale is 1 km for both clusters and triplets.

In order to minimize the uncertainty that comes from high aspect ratio triplets, we subsample the data set, selecting only quasi-equilateral and nonoverlapping triangle configurations. The procedure is applied separately at different spatial scales. As a metric for triangle aspect ratio, we choose the parameter

$$\Lambda = 12\sqrt{3}\frac{A}{P^2}, \tag{6}$$

where P is the perimeter. Λ is normalized so that $\Lambda = 0$ for collinear points and $\Lambda = 1$ for equilateral triangles. Given a prescribed scale separation bin, $[l^{\min}, l^{\max}]$, and a time averaging interval (here 1 hr), at the start of each interval we find all possible drifter triplets with all sidelengths in $[l^{\min}, l^{\max}]$ and order these by their Λ value. Any triplet with $\Lambda < 0.7$ is discarded. In addition, a triplet is removed from the ordered list if either (a) one of its drifters is a member of another triplet with higher Λ value (to ensure independence) or (b) it changes orientation during the time interval.

Estimates of the kinematic properties over the given time interval are computed for each triplet using Equations (3)–(5) and scaled by the local Coriolis parameter ($7.071 \times 10^{-5}\ s^{-1}$). The process is repeated, independently, for each averaging time interval and for each scale bin $[l^{\min}, l^{\max}]$. Data from the first 4 days after deployment are considered for the summertime S1 and S2 launches. For the wintertime W2 and W1 launches, the analysis window is reduced to 1 day to avoid strong storm events (and the associated large numbers of drogue losses). The significantly larger number of drifters launched in the winter deployments produced more samples despite the shorter analysis time span.

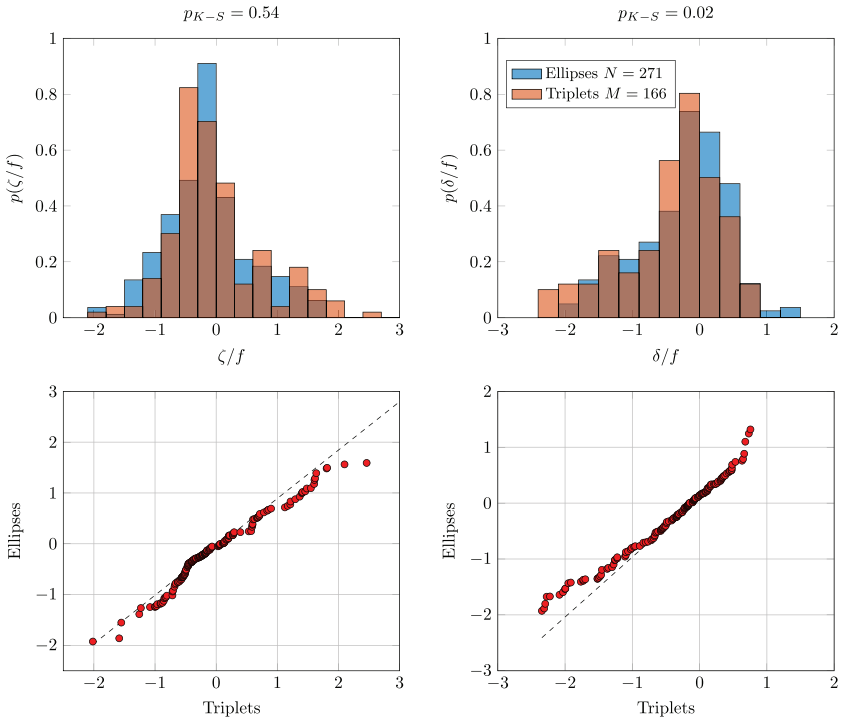

Figure 3. Top panels: Comparison of the distribution of observed vorticity (left) and divergence (right), derived from drifter triplets and larger clusters for the winter W2 (east) launch. Data corresponds to that shown in Figure 2. The estimated *p*-value from two-sample Kolmogorov-Smirnov hypothesis tests are shown in the titles. Lower panels: Corresponding quantile-quantile plots for the vorticity (left) and divergence (right).

2.5.2. Comparison of Gradient Estimates From Drifter Triplets and Larger Clusters

For least squares methods, clusters of $N > 3$ drifters are generally preferred to reduce errors (Essink, 2019; Ohlmann et al., 2017). Similar accuracy gains from increased numbers are not as obvious for convex-hull based algorithms, as what is used here. Therefore, the robustness of the triplet results is tested against least squares estimates from clusters with $N > 5$ drifters. Given a single drifter trajectory, $D^i(t)$, all drifters are collected that are located within a radius r at time t. The resulting group (including D^i) forms a cluster. Averages, this time over the cluster, will again be denoted with overbars. The velocity gradients at the cluster's mean position $(\overline{x}, \overline{y})$ can be estimated by least squares fits to the linear spatial expansions

$$\Delta u^i = \frac{\partial u}{\partial x}\Delta x^i + \frac{\partial u}{\partial y}\Delta y^i, \tag{7}$$

$$\Delta v^i = \frac{\partial v}{\partial x}\Delta x^i + \frac{\partial v}{\partial y}\Delta y^i, \tag{8}$$

where $\Delta x^i = x^i - \overline{x}$, $\Delta y^i = y^i - \overline{y}$, $\Delta u^i = u^i - \overline{u}$, and $\Delta v^i = v^i - \overline{v}$, and $(\overline{u}, \overline{v})$ is the mean velocity of the cluster (cf. Method I of Molinari & Kirwan 1975).

Figure 2 shows comparisons between cluster-based and triplet-based estimates of vorticity and divergence for the W2 launch. The top panels show the 1-hr mean locations of all available clusters with $N > 5$ drifters and radius $750\,\text{m} \le r \le 1.25\,\text{km}$ during the first 12 hr after the last drifter launch. An ellipse is fit to each cluster (Emery & Thomson, 1998) and colored by the scaled vorticity or divergence estimate. Following D'Asaro et al. (2018) and Ohlmann et al. (2017), results from highly anisotropic clusters are avoided by removing those clusters where the length of the major axis is greater than 5 times that of the minor axis. No attempt is made to ensure independence, and different clusters may share one or more individual drifters. As a consequence, there is considerable spatial overlap in the ellipses. The lower panels show the same for all available nonoverlapping, quasi-equilateral ($\Lambda \ge 0.7$) triplets with sidelengths in the range [750,1250] m as well. There is general agreement between the results from the two approaches.

The level of agreement is quantified in Figure 3 by comparing the vorticity and divergence distributions from each of the two methods. Standard two-sample Kolmogorov-Smirnov tests indicate that the vorticity

Table 1
Number of Non-Overlapping Samples in Each Scale-Bin for the Four Launches With Corresponding 1-Hr Average KP Statistics

$\langle r \rangle [l^{min}, l^{max}]$	Launch	N	$\langle \overline{\zeta} \rangle / f$	$\sigma^2_{\zeta/f}$	$\langle \overline{\delta} \rangle / f$	$\sigma^2_{\delta/f}$	$\langle \alpha \rangle / f$	$\sigma^2_{\alpha/f}$
	W1	226	1.36	5.36	-0.14	2.52	2.01	1.75
0.2 km	W2	402	-0.30	4.25	-0.13	2.64	1.99	1.52
[0.15, 0.25] km	S1	202	0.50	2.52	0.12	1.16	1.36	1.18
	S2	286	0.01	0.60	0.07	0.56	0.99	0.38
	W1	867	1.14	2.50	-0.22	1.10	1.44	1.52
0.5 km	W2	921	-0.15	1.42	-0.22	1.26	1.39	0.97
[0.4, 0.6] km	S1	357	0.41	0.88	0.04	0.54	0.82	0.42
	S2	328	0.05	0.37	-0.10	0.40	0.72	0.23
	W1	1357	1.01	1.76	-0.18	0.43	1.11	0.65
1 km	W2	832	-0.12	0.56	-0.18	0.46	0.94	0.53
[0.75, 1.25] km	S1	227	0.41	0.37	-0.00	0.29	0.80	0.58
	S2	99	0.04	0.15	0.00	0.26	0.62	0.11
	W1	1734	1.13	1.34	-0.14	0.25	0.84	0.39
2 km	W2	1135	-0.19	0.07	-0.10	0.23	0.65	0.21
[1.5, 2.5] km	S1	220	0.26	0.07	-0.04	0.12	0.70	0.34
	S2	97	0.00	0.05	0.08	0.06	0.44	0.04
	W1	1525	0.63	0.63	-0.08	0.09	0.64	0.18
3 km	W2	916	-0.21	0.09	-0.03	0.12	0.47	0.10
[2.5, 3.5] km	S1	258	0.31	0.18	-0.06	0.16	0.65	0.20
	S2	114	-0.06	0.07	0.05	0.09	0.40	0.04
	W1	1403	0.81	0.39	-0.04	0.07	0.50	0.10
4 km	W2	724	-0.19	0.06	0.02	0.09	0.44	0.09
[3.5, 4.5] km	S1	260	0.18	0.09	-0.03	0.08	0.43	0.11
	S2	98	0.00	0.05	0.00	0.13	0.49	0.04
	W1	1250	0.80	0.25	0.02	0.07	0.43	0.07
5 km	W2	689	-0.18	0.05	0.07	0.08	0.44	0.09
[4.5, 5.5] km	S1	397	0.11	0.08	0.03	0.05	0.32	0.05
	S2	133	0.01	0.06	0.01	0.12	0.49	0.04

Note. Shaded rows correspond to data displayed in Figures 10 and 11. Winter launches are W1 (west) and W2 (east); summer launches are S1 (west) and S2 (east).

estimates are likely drawn from the same distribution. The p value for the divergence, on the other hand, is very small, although still significant. As shown in the lower right panel, the divergence distributions are similar except for a slightly heavier negative tail and reduced positive tail in the triplet case. Some of these differences could be due to differential spatial sampling; some of them can be ascribed to the differences in what is being estimated (area-averaged versus point values).

2.5.3. Validation of Drifter Estimates: Comparison With X-Band Observations

Drifter triplet estimates are also compared with independent kinematic property estimates obtained from Eulerian X-band radar data. The Eulerian X-band radar observations collected during the winter experiment provide independent observations to test the accuracy and robustness of the drifter-based estimates of surface vorticity and divergence. The inhomogeneous spatial sampling by the drifters is expected to be biased toward convergence regions, and the comparison is therefore limited to simultaneous (within a ±1.5-hr window) and colocated estimates from both sources. Drifter-based estimates are drawn from the 1-km bin to approximately match the triangle area with the area of the minimal Eulerian radar grid-box $\Delta x \approx 500$ m. (The subsampling results in small differences with the statistics presented in Table 1.) Some discrepancies between estimates are expected, since the Eulerian fields result from temporal/spatial smoothing and

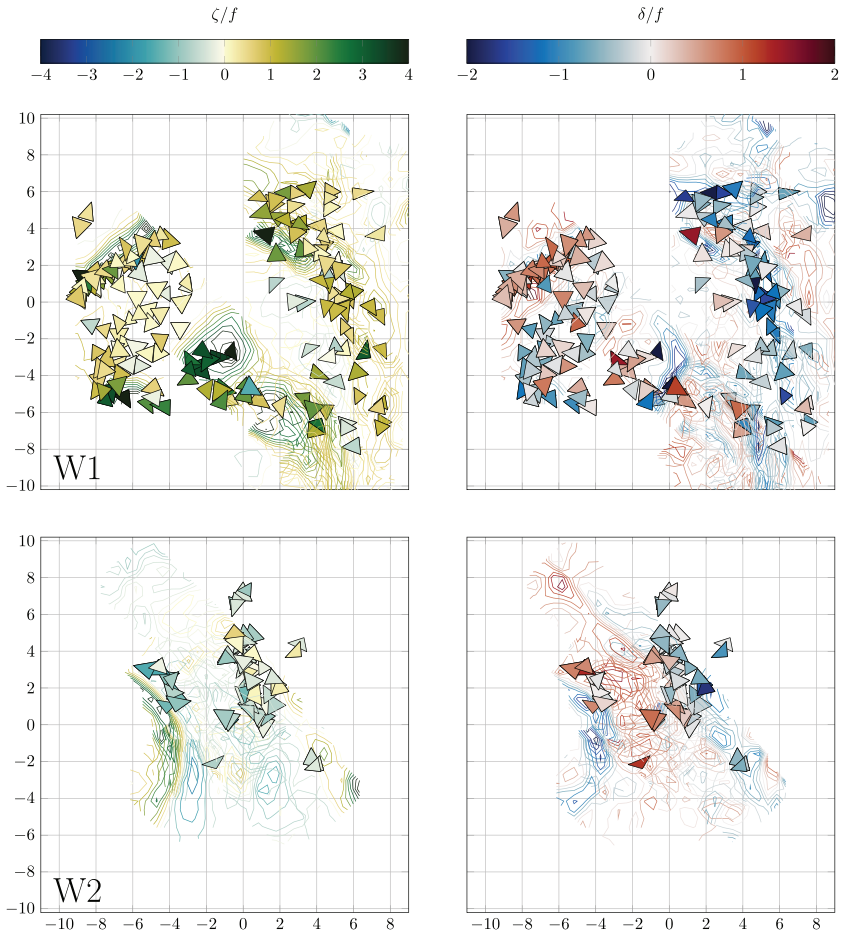

Figure 4. Comparison of the wintertime surface kinematic properties from along-track X-band radar data (overlapping contours) and 1-hr averaged estimates from nearly equilateral drifter triplets with side length in the 1-km bin (colored triangles). Left panels show comparisons of scaled vertical vorticity, ζ/f, and right panels scaled divergence, δ/f, for W1 (west, top) and W2 (east, bottom). Horizontal distances are shown in kilometers.

projection onto the grid and are thought to be representative of currents deeper than those sampled by the drifters (Lund et al., 2018).

Comparisons of the vorticity and divergence estimates from the two data sets are given in Figure 4 for western W1 (top) and eastern W2 (bottom) deployments. Each panel shows the location of drifter triplets colored by the 1-hr averaged vorticity and divergence estimate for that triplet. The drifter based estimates are superimposed on contours of vorticity and divergence computed from corresponding swaths of radar images. Data from all possible sample times are plotted together. Despite the completely independent nature of the two sets of observations and the distinct differences in the spatial resolution of the surface field, the vorticity and divergence estimates agree remarkably well at the majority of spatial locations.

To produce direct, quantitative comparisons between drifter and radar observations, coincident measurements were found. For each hourly averaged drifter triplet, we find any radar measurement that occurred during that hour and interpolate the radar estimates to the mean drifter triplet position. For the 1-km-scale bin, this gives 90 coincident measures for W1, and 31 for W2. A scatter plot of the resulting Eulerian and drifter-derived kinematic property estimates is given in Figure 5. Comparisons of the estimated means, variances, and skewness of the distributions are given in Table 2.

While there is considerable scatter between the two methods, there is relatively strong correlation and minimal offset. Vorticity means and standard deviations agree across both experiments with both observational

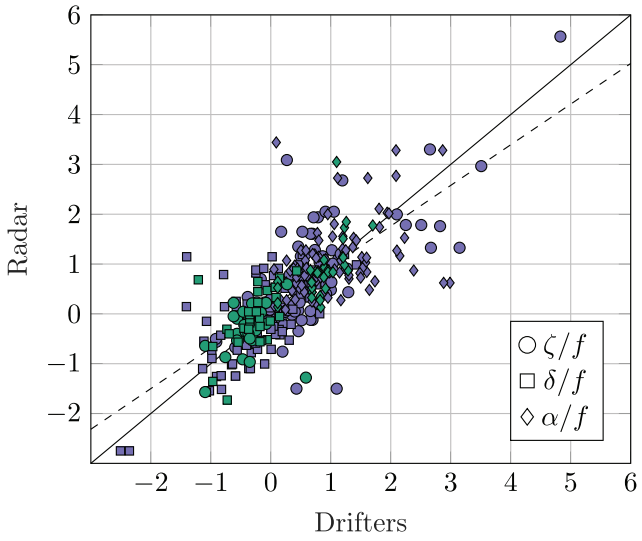

Figure 5. Scatter plot of velocity gradient estimates obtained from coincident drifter triplet and X-band radar observations for winter W1 (west, purple) and W2 (east, green) launches. Dashed line shows best fit linear estimate, $y = 0.82x + 0.13$, with $R^2 = 0.75$ over both launches and all three kinematic properties.

methods detecting similar skewness in both vorticity and divergence in W1. Both drifter and radar-based observations show consistent differences between the two launches, even though there are quantitative differences in the specific values. Uniformly across launches and gradient metrics, drifter-based measurements show larger variances. This is likely a consequence of the inherent smoothing of the radar-derived velocity field.

2.6. Energy Metrics From Two-Point Drifter Statistics

The energetic properties of the four launches are characterized using standard particle-pair statistics. The scale dependence of the fluctuations in the surface velocity field can be estimated from moments of the two-point longitudinal velocity increment (Kolmogorov, 1941; LaCasce, 2008; Poje et al., 2014)

$$\Delta u_l(\mathbf{r}, \mathbf{x}, t) = (\mathbf{u}(\mathbf{x} + \mathbf{r}, t) - \mathbf{u}(\mathbf{x}, t)) \cdot \frac{\mathbf{r}}{||\mathbf{r}||}, \tag{9}$$

which measures the velocity difference at time t between two points separated by $\mathbf{r}$ in the direction of the separation vector. Similarly, the transverse increments, measuring velocity differences orthogonal to the separation vector, are defined by

$$\Delta u_t(\mathbf{r}, \mathbf{x}, t) = (\mathbf{u}(\mathbf{x} + \mathbf{r}, t) - \mathbf{u}(\mathbf{x}, t)) \times \frac{\mathbf{r}}{||\mathbf{r}||}. \tag{10}$$

The longitudinal and transverse structure functions are defined by the moments of the increments:

$$S^n_{l,t}(r) = \langle \Delta u^n_{l,t}(\mathbf{r}, \mathbf{x}, t) \rangle \tag{11}$$

for any exponent n, where $\langle \cdot \rangle$ denotes an average over $\mathbf{x}$ and t. Assuming homogeneity, isotropy, and statistical stationarity, the structure functions depend only on the distance between points $r = ||\mathbf{r}||$. These assumptions clearly have limited applicability in submesoscale ocean flows. Therefore, we will restrict our analysis to 24-hr windows following the release of the last drifter and treat each drifter launch separately.

The spatial and temporal density of the drifter data permits estimates of the Eulerian quantities, $S^n_{l,t}(r)$, by treating the drifter data sets at any time as (spatially inhomogeneous, conditionally sampled by the advecting flow) Eulerian field measurements (Poje et al., 2017). For each available drifter pair, $\Delta u_{l,t}(\mathbf{r}, \mathbf{x}, t)$ is calculated at each time, and statistics are obtained by averaging the data conditioned on binned separation distances.

3. Environmental Conditions of the Four Drifter Launches and Eulerian Surface Velocities

During both the summer and winter experiments, the Loop Current's northern extent was well south of the area of interest outlined in Figure 1a. In June 2012, a Loop Current Ring was detached but remained south of 27°N, while in January–February 2016, the Loop Current was extended north to ~26.5°N (see the sea surface height product of R. Leben at https://geo.gcoos.org/ssh/). The general flow patterns of each launch as given by the full set of drifter trajectories are shown in Figure 6.

Table 2
Mean, Variance, and Skewness of the Distributions of Vertical Vorticity and Horizontal Divergence for Coincident Drifter-Based and Radar-Based Estimates

Launch	Source	$\langle\zeta\rangle/f$	$\sigma_{\zeta/f}$	$\text{skew}_{\zeta/f}$	$\langle\delta\rangle/f$	$\sigma_{\delta/f}$	$\text{skew}_{\delta/f}$	$\langle\alpha\rangle/f$	$\sigma_{\alpha/f}$
W1	Drifters	0.71	1.04	1.39	-0.12	0.82	-0.66	1.07	0.69
	X-Band	0.70	0.91	1.90	-0.20	0.67	-0.55	1.02	0.67
W2	Drifters	-0.34	0.46	-0.59	-0.09	0.58	-0.69	0.88	0.60
	X-Band	-0.39	0.32	0.52	-0.30	0.36	-0.58	0.86	0.37

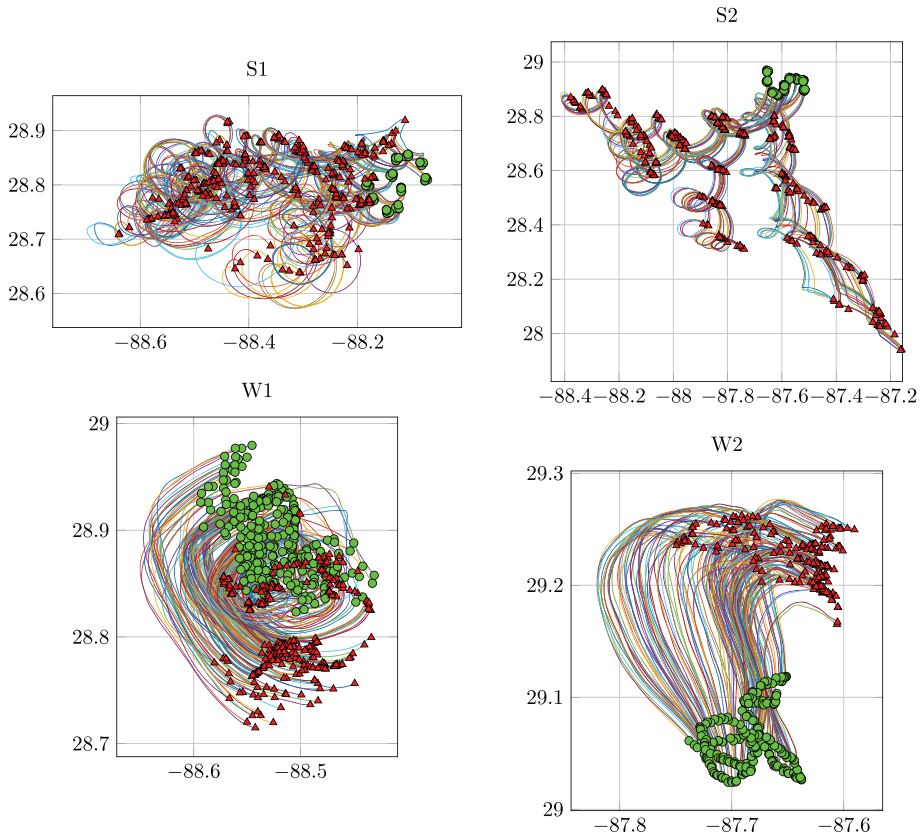

Figure 6. Drifter trajectories in the four experiments (96 hr trajectories for the summer launches, 24 hr for the winter launches). Green circles indicate position at time of the last drifter launch in each experiment. Red triangles show daily positions from this time.

The two summer deployments, S1 (west) and S2 (east), from July 2012 were characterized by relatively weak winds, with typical speed of ~5 m/s, and drifter trajectories show marked inertial oscillations (Figure 6), as previously observed by Beron-Vera and LaCasce (2016), due to the shallow summer mixed layer. The two deployments were purposefully targeted to observe distinct flow fields (Berta et al., 2016; Poje et al., 2014). The S1 launch covered an area of weak westward mean drift in a region with small, submesoscale frontal structures, while S2 was launched across a strong southward jet. Observations of the local water mass properties from CTD casts are presented in Figure 7. The 30-m depth profiles of potential density, salinity, and temperature for each individual CTD cast have been arranged from the west to the east. As expected, the summer mixed layer is shallow with large density variations confined within the first 10 m. The S2 launch occurred in warm water with nearly horizontally uniform temperature, but across a single, relatively strong salinity-induced density front. In contrast, the western launch (S1) occurred in cold, fresh water marked by multiple small-scale near-surface horizontal density gradients produced by freshwater filaments and subsurface intrusions of warm water.

The winter experiment was conducted during an El-Niño winter (January–February 2016), and the weather was characterized by the passage of several severe storms with winds exceeding 15 m/s. The average wind speed over the 2-month period was ~8 m/s. The W2 deployment targeted the general area near the corresponding summer launch (S2) and took place immediately prior to the passage of a strong weather system with winds exceeding 15 m/s and veering strongly from south-eastward to north westward about 20 hr after launch. The mean drifter trajectories shown in Figure 6 reflect this abrupt change of wind forcing of the surface currents in the W2 launch. Meanwhile, the western winter deployment (W1) specifically targeted an energetic cyclonic structure ~15–20 km in diameter located in the western DeSoto Canyon. The organized cyclonic motion and spatial extent of the feature are evident in the sampled drifter trajectories in Figure 6. The wind during the deployment and the following 24 hr analysis period remained steady at

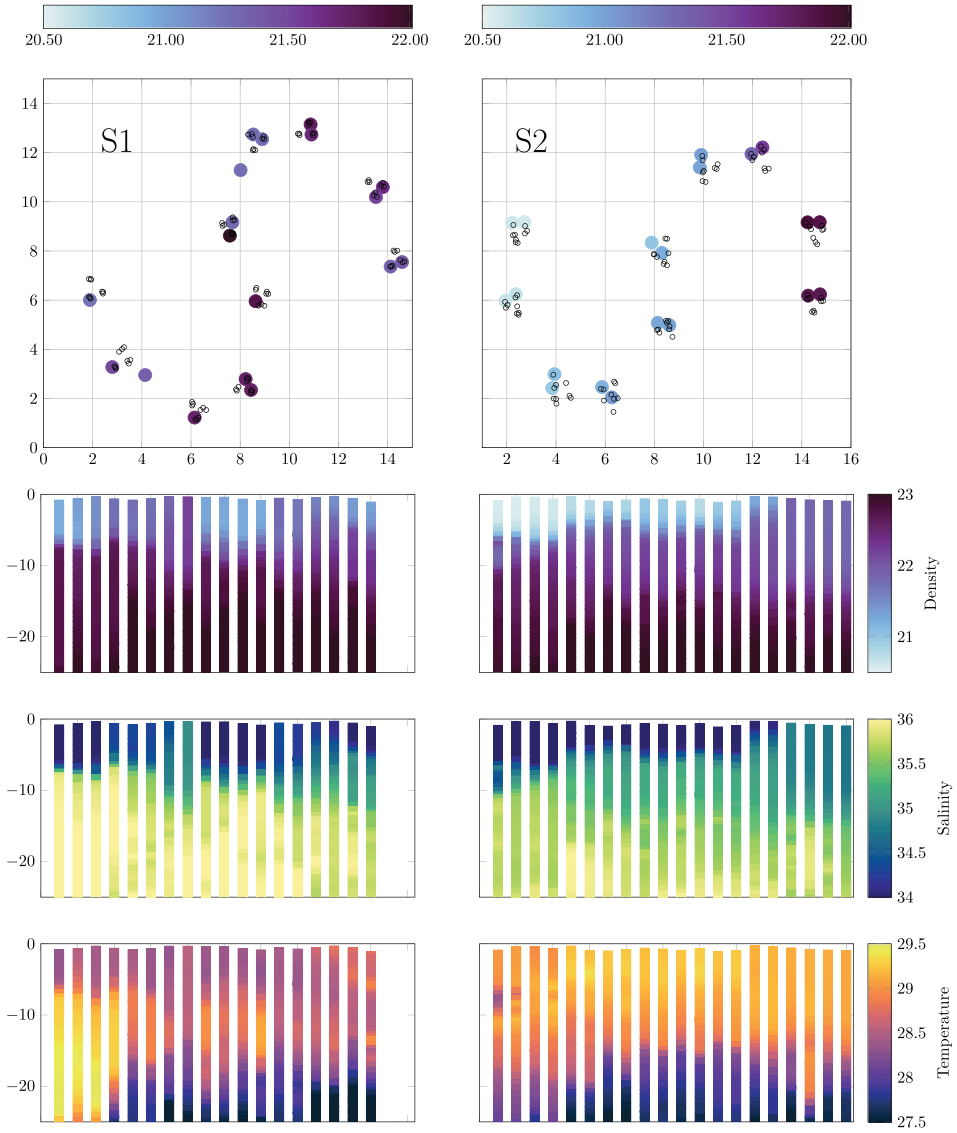

Figure 7. Top panels show locations of drifter launches (black circles) and CTD casts (colored by potential density) during summer S1 (west, left) and S2 (east, right) experiments. Bottom panels show, ordered from west to east, the observed depth dependence of potential density, salinity, and temperature in the two launches. Vertical axes show depth in meters.

~8 m/s. The subsequent evolution, 1 week after the passage of another frontal weather system, resulted in the remarkably strong convergence event studied by D'Asaro et al. (2018).

Figure 8 shows the near-surface MVP CTD data collected during the two winter launches. The top panels show the drifter launch locations colored by density extrapolated from the nearest available observations along the full launch time surveys. The lower panels show vertical profiles, to 100 m, of potential density, salinity, and temperature taken along the single horizontal transect indicated in the top panels. Although the mixed layer depth is approximately 80 m in both instances, the two launches sampled markedly different water masses, W1 (west) in cold, fresh water associated with the Mississippi River and W2 (east) in warm, salty Gulf of Mexico shelf water. Profiles across W1 indicate a salinity-compensated density structure, with relatively strong horizontal surface density gradients produced by filaments of cold, fresh water extending to 20–40 m deep, similar to the observations during the corresponding western summer launch (S1). These are submesoscale structures, with a horizontal length scale of the filaments <1 km. In contrast, the horizontal density structure during the W2 launch is nearly uniform over the launch pattern, with indications of a freshwater front located 6–8 km to the west of the drifter deployment.

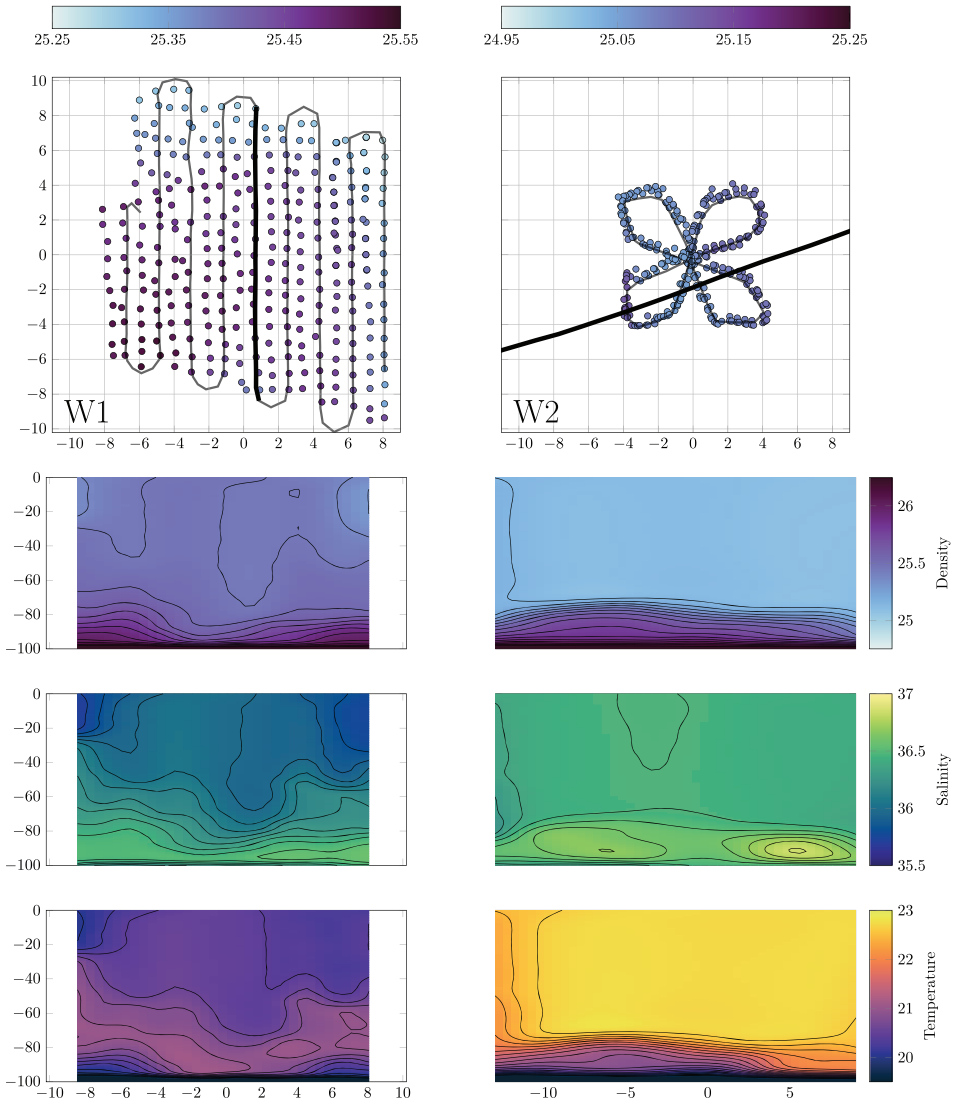

Figure 8. Top panels show the winter drifter launch locations for W1 (west, left) and W2 (east, right), colored by interpolated values of near surface potential density taken along the ship track (thin, gray trajectory) at launch times. Note that drifters were released from two ships traveling in parallel lines, but only one was equipped with hydrographic equipment. Horizontal axes are in kilometers. Lower panels show vertical profiles of density, salinity, and temperature structure from individual transects (bold, black lines in top panels) through the deployments. Vertical axes show depth in meters, horizontal axes in kilometers along transects.

The hydrographic information for the winter launches is complemented by the X-band radar observations taken during the two drifter deployments. Figure 9 shows a compilation of several snapshots of the near-surface vorticity (left panels) and divergence (right panels) during the winter experiments derived from the X-band radar observations. The kinematic properties are computed using finite differencing of the velocity field with 480 m spatial resolution. The horizontal grids in Figure 9 are in kilometers centered on the center of mass of each drifter deployment. The maximum temporal offset of the snapshots combined for each panel is ~3 hr.

The strong cyclonic feature targeted by the W1 (west) launch is clearly evident in the X-band observed surface vorticity, with a core well in excess of $5f$. Associated with the cyclonic core is a region of strong horizontal convergence. Other structures and filaments are visible in the vorticity and divergence fields, confirming the influence of surface filaments of cold, fresh water associated with the Mississippi River, as shown in Figure 8. The situation is quite different for W2 (east). The observed velocity gradient fields in the center of the launch show a quasi-homogeneous region of negative vorticity ($\zeta/f \geq -1$) with mostly

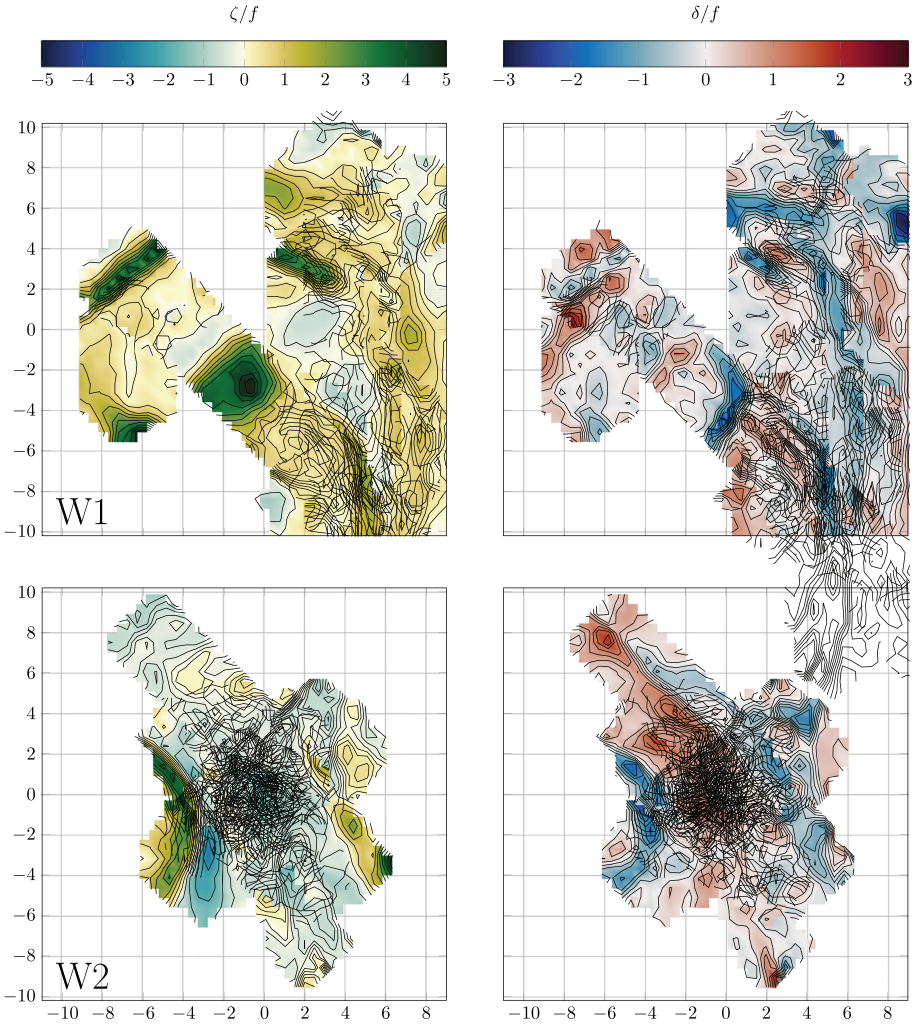

Figure 9. Surface kinematic properties during the winter launches from along ship-track X-band radar data. Left panels show estimates of scaled vertical vorticity, ζ/f, during W1 (west, top) and W2 (east, bottom). Right panels show, from the same observations, the scaled surface divergence, δ/f, in the winter launches. Horizontal grids are in kilometers.

positive divergence, while large cyclonic vorticity ($\zeta/f > 4.5$) and associated large surface convergence can be seen in the region of the salinity front to the southwest of the drifter deployment indicated in the CTD transects. The W2 drifters, though, did not sample this feature.

In summary, the hydrographic data show a seasonal mixed layer of ~80 m in winter and ~10 m in summer, as expected. In addition, both seasons are characterized by spatial inhomogeneity across the DeSoto Canyon due to the Mississippi River outflow. Both the summer S1 and the winter W1 deployments in the western region of the Canyon influenced by Mississippi River outflow, show complex near-surface horizontal density structures produced by evolving filaments of cold-fresh water, that are absent in the more eastern S2 and W2 launches.

4. Drifter-Based Surface Kinematic Properties

4.1. Velocity Statistics

The mean Lagrangian velocity components and magnitude for the first hour following completion of each deployment is shown in Table 3, along with the number of drifters with usable data. The summer S2 (east) launch, deployed along a mesoscale frontal jet flowing to the south southwest, has considerably larger mean advection speed than any of the other cases (almost 70 cm/s). The mean speed for S1, the summer

Table 3
Number of Drifters and 1-Hr Average Velocity for Each Launch

Experiment	Launch	N	$\langle u \rangle$ (cm/s)	$\langle v \rangle$(cm/s)	Mean speed (cm/s)
Wwinter	W1 (west)	326	-23.8	-13.0	27.2
	W2 (east)	300	-4.2	34.6	34.8
summer	S1 (west)	89	2.0	-7.1	7.3
	S2 (east)	90	-4.9	-69.4	69.5

deployment in the western canyon, is considerably lower (by almost a factor of 10). The winter values are both around 30 cm/s, with W1 (west) slightly lower and the W2 (east) velocity components reflecting the northward direction of the increasingly strong mean wind during and immediately after deployment.

4.2. Scale-Dependence and Seasonality of Surface Kinematic Property Statistics

The methodology introduced in section 2.5.1 is used here to quantify properties of surface velocity gradients across multiple length-scales in the submesoscale range for the four drifter launches. The total number of nonoverlapping, 1-hr averaged drifter triplets available in the separate scale bins is given in Table 1, together with the corresponding mean and variance estimates for $\overline{\zeta}$, $\overline{\delta}$, and $\overline{\alpha}$. The effects of sampling scale on the distributions of vorticity and divergence across the four experiments are explored in Figures 10–13. The distributions of 1-hr averaged kinematic properties for all drifter triplets within a deployment in the 500-m and 2-km bins are superimposed in Figures 10 and 11 for vorticity and divergence, respectively. Comparisons of the vorticity distributions, quantified by mean and skewness, across a range of separation scales are given in Figure 12. Error bars show the 95% confidence intervals estimated by bootstrapping on 500 samples in each case. Figure 13 displays the variances for both vorticity and divergence.

While the mean vorticity shows little scale dependence for summer S2 (east) and hovers around 0 at all scales, the other launches show a general weakening trend for increasing scales, with negative values

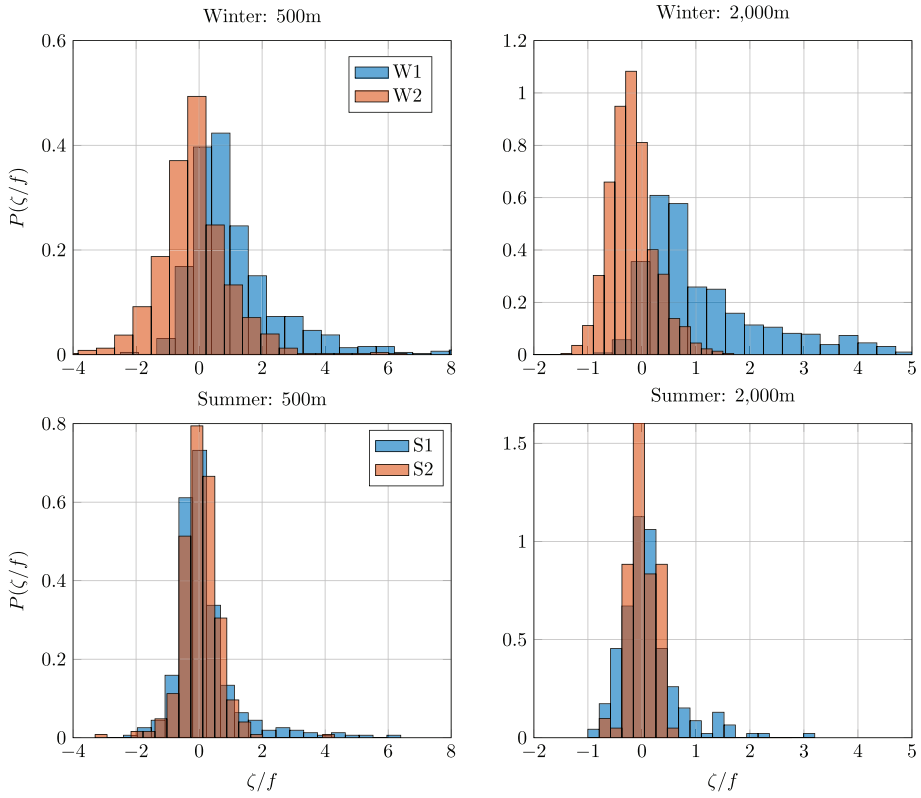

Figure 10. Distributions of 1-hr time-averaged scaled vorticity estimates for the winter launches (top) and the summer launches (bottom) computed from drifter triplets with length-scales 500 m (left) and 2 km (right).

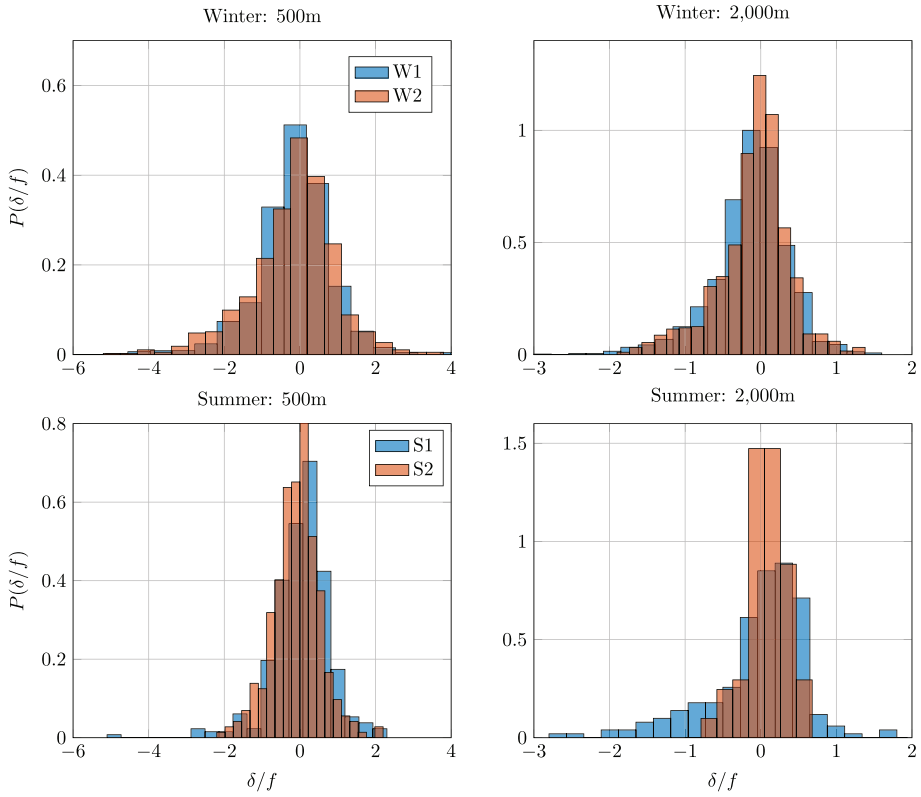

Figure 11. Distributions of 1-hr time-averaged scaled divergence estimates for the winter launches (top) and the summer launches (bottom) computed from drifter triplets with length-scales 500 m (left) and 2 km (right)

for winter W2 (east) and positive values for the two western deployments W1 (winter) and S1 (summer) (Figure 12a). This is consistent with the larger averaging area implied by the larger scales. As expected from a launch targeting a strong vortex, W1 shows higher values across all scales. Scale-dependence all but disappears in the eastern winter launch (W2) for scales >1 km, reflecting reduced variability at these scales in constrast to both the summer and winter launches to the west (S1, W1). In this regard, W1 is more similar to S1—the other western launch influenced by the Mississippi River outflow—than either to the respective other launches of the same season. This can also be observed in the vorticity skewness (Figure 12b). W1 and S1, launched in locations with small-scale horizontal density gradients produced by filaments of freshwater, both show significant vorticity skewness at scales up to 2 km. These long tails at high vorticity values reflect the impact of the freshwater intrusions. At the 1-km scale, skew$(\zeta/f) \approx 2.5$ for S1, comparable to the value of 2.52 reported by Shcherbina et al. (2013) from two-ship ADCP measurements at 1-km

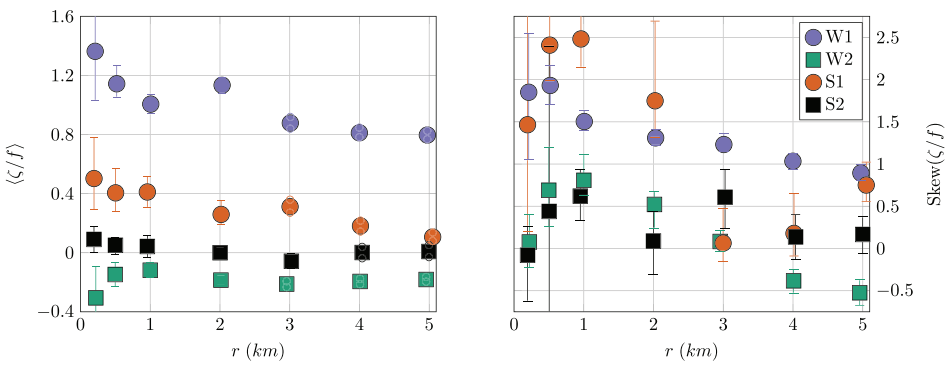

Figure 12. Scale dependence of the triplet-derived (a) mean and (b) skewness of the vorticity distribution for the four launches. Error bars show the 95% confidence interval from bootstrapping on 500 samples.

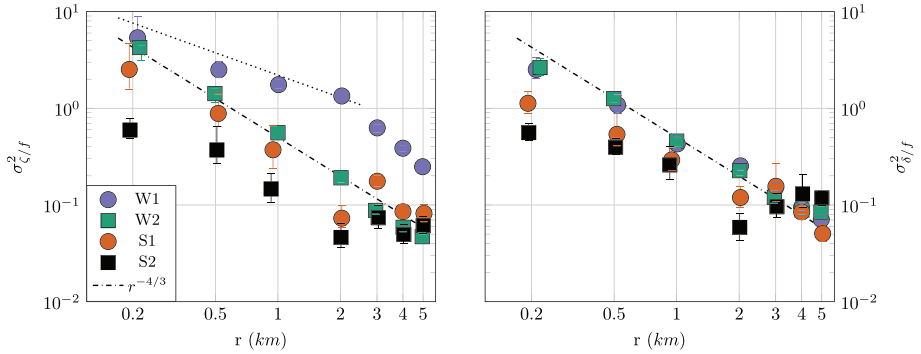

Figure 13. Scale dependence of the variance of the distributions of (a) vorticity, $\sigma^2_{\zeta/f}$, and (b) divergence, $\sigma^2_{\delta/f}$, in the four launches. For comparison, the scaling laws for velocity derivatives are also shown as a dash-dotted line for $\sigma^2 \sim r^{-4/3}$ and a dotted line in (a) for $\sigma^2 \sim r^{-4/5}$.

separation scale taken in the vicinity of the Gulf Stream. For W1, skew$(\zeta/f) \approx 1.5$, but the eastern launches, in both seasons, show significantly lower levels of vorticity skewness. Unlike the western winter launch (W1) where skew$(\zeta/f) > 1$ persists beyond 3-km sampling, significant vorticity skewness is confined to smaller scales in the corresponding summer S1 launch where the signal decays rapidly for triplets with side-lengths larger than 2 km. This may well reflect the particular conditions of the energetic vortex sampled by the W1 deployment.

In contrast to the vorticity (Figure 10), the distributions of divergence (Figure 11) at 500 m scales are similar in all four cases, with larger ranges in the winter launches, although summer S1 (west) is unique in that it has a positive mean. At 2 km, the divergence distributions in W1, W2, and S1 are also qualitatively similar. At this separation scale, the eastern summer deployment (S2) stands out with positive mean and significantly smaller variance than the other launches.

In all the launches, the widths of the distributions of both $\overline{\delta}$ and $\overline{\zeta}$ decrease with increasing observation scale, consistent with peak values being averaged out over larger scales. This scale dependence is quantified in Figure 13, where the vorticity and divergence variances are plotted against separation scale on log-log axes. The winter W1 (west) launch, directed at the center of an energetic cyclone, has at all observation scales the largest vorticity variance and also shows the slowest decay with separation scale in the 0.5–2 km range. Summer S2 (east), on the other hand, has the lowest vorticity variance among all deployments, especially at small scales.

Seasonal differences are more pronounced in the divergence variance estimates (Figure 13b) that show wider distributions in winter up to scales of 2 km and very little variation between the two winter deployments. Winter conditions, with a deeper mixed layer and more energetic wind forcing, produce more extreme divergence values. The results for $\sigma^2_{\delta/f}$ at 200 and 500 m for summer S1 and S2 are consistent with those reported for the mean-square divergence in Berta et al. (2016) estimated from the evolution of initial launch triplets over a 12-hr analysis window.

In summary, the statistics for the two western launches subject to freshwater intrusions, winter W1 and summer S1, are consistent with the limited number of direct observations of gradient properties in developed submesoscale near-surface turbulence (Buckingham et al., 2016; Shcherbina et al., 2013) and also compatible with results from submesoscale resolving models (Capet et al., 2008b). The vorticity distribution is heavily skewed to the right, the divergence distribution is more heavily skewed toward negative values, and the motion is highly ageostrophic, with significant probability of observing local vorticity (computed over 500-m scales) in excess of 3–4 f. The winter W2 (east) launch has a markedly different vorticity distribution, with negative mean value, considerably less vorticity variance and skewness than winter W1 (west), and a very low probability of observing cyclonic vorticity above 2–3 f. The divergence distribution, on the other hand, is very similar for the two winter launches, W1 and W2, and exhibits a seasonal signature. The summer S2 (east) distribution shows very low average vorticity across all scales, from 200 m up to 5 km, and low levels of vorticity skewness. The narrow distribution of S2 kinematic properties across different scales suggests that the observed dynamics are driven by processes at scales larger than the triplets sizes considered, and that the mesoscale jet in which S2 is caught prevails over smaller scales.

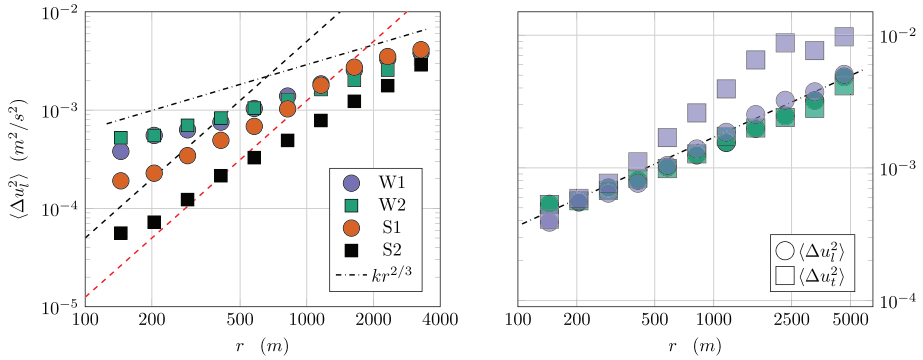

Figure 14. Scale-dependent two-point velocity differences computed for the four launches, over the first 24 hr after last drifter launch. (a) Scale-dependent fluctuating energy given by the longitudinal second-order structure function. The scaling law $S_l^2(r) \sim r^{2/3}$ is indicated by the dot-dashed line, and the dashed lines correspond to $\mathrm{Ro}_{\mathrm{loc}} = 1/2$ (red) and 1 (black). (b) Comparisons of the longitudinal (circles) and transverse (squares) structure functions for winter launches.

4.3. Comparing Scale Dependence of Kinematic Properties and Two-Point Velocity Increments

4.3.1. Drifter Pair Statistics

Results for the scale-dependent fluctuating energy in terms of the second-order longitudinal structure function, $S_l^2(r)$, for the four deployments are shown in the left panel of Figure 14. Energetically, the two winter launches are nearly indistinguishable with both exhibiting a shallow scaling law, $S_l^2(r) \sim r^k$, $k \approx 2/3$, consistent with a broadband wave number spectrum in the submesoscale range, and considerable energy at the smallest separation scales. Notably, the fluctuating energy in the summer S1 (west) launch shows greater similarity to the winter launches than to the eastern summer launch (S2), where, in comparison to the other experiments, significantly less energy at the smallest separation scales and a considerably steeper scaling law slope ($k > 1$) are observed.

The relative size of the velocity increments, and a coarse estimate of the degree of ageostrophy in the fluctuating field, can be determined by defining a local, scale-dependent Rossby number (Poje et al., 2017),

$$\mathrm{Ro}_{\mathrm{loc}}^2(r) = \frac{\langle \Delta u_l^2(r) \rangle}{f^2 r^2} \ . \tag{12}$$

As shown by the dashed lines corresponding to $\mathrm{Ro}_{\mathrm{loc}}(r) = 1$ (black) and $\mathrm{Ro}_{\mathrm{loc}}(r) = 1/2$ (red) in the figure, local Rossby numbers remain above 1/2 in the W2, W1, and S1 launches at 1 km scales and below, while the fluctuations observed in summer S2 (east) are considerably less ageostrophic.

The right panel of Figure 14 shows the longitudinal and transverse structure functions $S_l^2(r)$ and $S_t^2(r)$ for the winter W1 (west) and W2 (east). Standard inertial range turbulence models, based on rough dimensional analysis, predict identical scaling laws for both structure functions. The results in Figure 14 indicate that while this is consistent with the observations in the W2 (east) launch (and similarly for both summer launches, not shown for clarity), it is not the case, at least for the scales above 500 m, in the W1 (west) observations.

Further comparisons of the distributions of drifter-derived velocity increments are given in Figure 15, which shows the scaled negative third moment, $-S_l^3(r)/r$, with dimensions of an energy dissipation rate. Only positive values are plotted. Under standard 3-D turbulence assumptions (Frisch, 1995; Kolmogorov, 1941), $S_l^3(r)$ is negative and scales with the separation distance in the inertial subrange. In this range, $-S_l^3(r)/r$ is a positive constant directly proportional to the forward energy cascade rate via Kolmogorov's 4/5 law. The values for both winter launches and the summer S1 (west) launch are roughly similar, and all three launches show reasonable scaling with nearly constant, positive values for separation scales less than 2 km. At scales larger than 3 km, both winter launches show $\Delta u_l(r)$ distributions with small, positive skewness ($S_l^3(r) > 0$). The results for the summer S2 (east) are markedly different, the value of the scaled third moment is an order of magnitude less than in the other cases, and $S_l^3(r)/r$ is negative only at the smallest separation scales.

In summary, the results consistently show that the properties of the near-surface velocity field as observed by two-point statistics of the drifters in the summer S2 (east) deployment, which was launched over an energetic

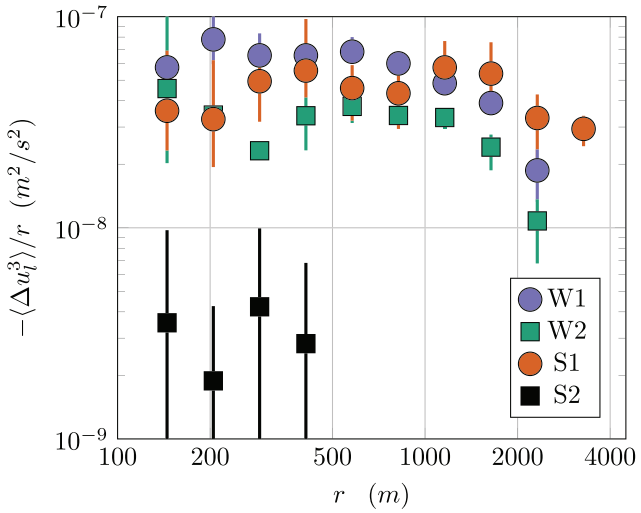

Figure 15. The scaled, sign-reversed, third-order longitudinal structure function for the four launches. Only positive values are plotted. Vertical lines show bootstrapped 95% confidence intervals.

jet, are markedly different from those observed in the other three cases. There is considerably less energy in the submesoscale band, steeper scaling law slope, and marginal ageostrophic signature, consistent with mesoscale, quasi-geostrophic dynamics, as indicated also by previous studies (Beron-Vera & LaCasce, 2016; Berta et al., 2016; Olascoaga et al., 2013). The results of the other three deployments, on the other hand, show higher-energy values at small scales, deviation from geostrophy at scales of 1 km, and negative and approximately constant scaled third-order moment. All these signatures are consistent with a broadband wave number spectrum and 3-D turbulence like dynamics in the submesoscale range.

4.3.2. Linking Kinematic Properties and Structure Functions

Rough estimates of the scale dependence of the variance of the velocity gradients can be made based on the scaling exponent β of the second-order structure functions, $S^2_{l,t}(r) \sim r^{\beta_{l,t}}$ (Kawai, 1985a). For an idealized eddy with length-scale r, the local divergence and vorticity are given by

$$\delta \approx \frac{\Delta u_l(r)}{r} \text{ and } \zeta \approx \frac{\Delta u_t(r)}{r} . \tag{13}$$

Upon averaging, the corresponding variances satisfy

$$\sigma^2_\delta(r) \sim \frac{S^2_l(r)}{r^2} \sim r^{\beta_l - 2} \quad \text{and} \quad \sigma^2_\zeta(r) \sim \frac{S^2_t(r)}{r^2} \sim r^{\beta_t - 2} . \tag{14}$$

Kawai's attempt to fit standard turbulence scaling following Kolmogorov (1941), $S^2_l(r) \sim S^2_t(r) \sim (\varepsilon r)^{2/3}$, to available ocean surface observations of $\sigma^2_{\delta,\zeta}(r)$ showed general agreement over the gross, six-decade range of scales, but very little coherent signal within the scale-range of any single set of observations (Kawai, 1985b). In contrast, the scaling of $\sigma^2_{\delta,\zeta}(r)$ in the present set of observations is clear enough (albeit only over a limited subset of submesoscale separation distances) to test how well scale-dependent gradient measures are predicted by two-point statistics. As shown in Figure 14a, $S^2_l(r) \sim r^{2/3}$ in both winter launches, implying the divergence variance should scale as $\sigma^2_\delta(r) \sim r^{-4/3}$ in winter W1 and W2. The dot-dashed line in Figure 13b indicates reasonable agreement between observations and this estimate. In addition, the progressively shallower decay of σ^2_δ observed in the summer launches S1 and S2 is consistent with the observations of progressively increasing scaling exponents for $S^2_l(r)$ in these two experiments.

The connection between the scale-dependence of the vorticity variance and the behavior of the transverse structure function is also apparent. Figure 14b indicates that while $\beta_l = \beta_t \approx 2/3$ for the winter W2 (east) launch, due to the significant effects of the large background vorticity in the flow, $\beta_t > \beta_l$ in the winter W1 (west) experiment. Figure 13a shows that $\sigma^2_\zeta(r)$ in W2 (and summer western S1) is well predicted by the $r^{-4/3}$ estimate. In the W1 launch, best fit estimates of $S^2_t(r)$ within the 300 m to 2 km range give $\beta_t = 1.2 \pm 0.005$, corresponding to a significantly slower, $\sigma^2_\zeta(r) \sim r^{-4/5}$ (shown by the dotted line in Figure 13a), vorticity variance decay, matching the direct observations. For both vorticity and divergence, there is close agreement between the drifter-triplet-based estimates of velocity gradients and the scaling behavior of standard two-point velocity increments.

4.4. Structure of Velocity Gradients: Eddy Versus Strain Dominance

As a means of distinguishing the structure of submesoscale turbulence in the four launches, we investigate the observed velocity gradient matrix. Kinematically, $\Delta\mathbf{u}$ determines the evolution of infinitesimal line elements. With $\boldsymbol{\delta x} = \mathbf{x}_2 - \mathbf{x}_1$, $||\boldsymbol{\delta x}|| \ll 1$,

$$\dot{\boldsymbol{\delta x}} = \mathbf{u}(\mathbf{x}_2, t) - \mathbf{u}(\mathbf{x}_1, t) = \nabla\mathbf{u}\ \boldsymbol{\delta x}, \tag{15}$$

and the nature of the motion is determined by the sign of the discriminant

$$\delta^2 - 4\ \det(\nabla\mathbf{u}) = \alpha^2 - \zeta^2, \tag{16}$$

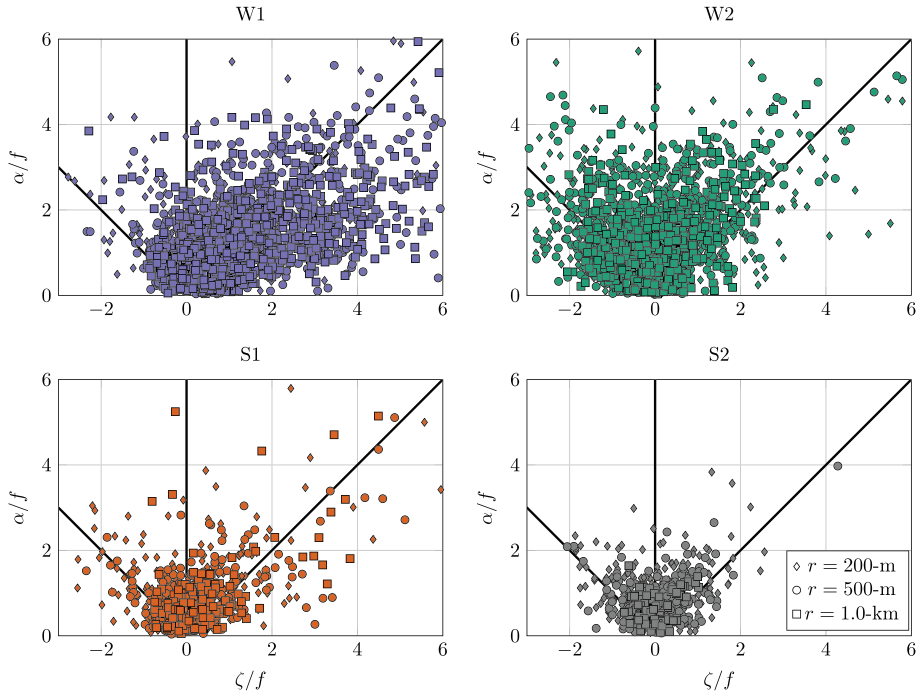

Figure 16. Scatter plots of normalized strain versus normalized vorticity in each of the four experiments, winter W1 (west) and W2 (east) and summer S1 (west) and S2 (east). Data is taken from 200-m (diamonds), 500-m (circles), and 1-km (squares) scale-bins in each.

where the strain is defined by $\alpha^2 = \left(u_x - v_y\right)^2 + \left(u_y + v_x\right)^2$. Given this, the curve $\alpha = |\zeta|$ marks the boundary between eddies, where vorticity dominates strain, and stretching regions, where the opposite is true (Hua & Klein, 1998; Okubo, 1970; Weiss, 1991).

Figure 16 shows scatter plots of the strain versus vorticity in the four flows derived from triplets in the 200 m to 1 km bins. The two winter launches (top) show significant differences. W1 (west) is dominated by cyclonic eddies (positive $\zeta > \alpha$), and α tends to increase with increasing ζ, suggesting that strain is more important at high vorticity. W2 (east), on the other hand, has very few cyclonic eddies, with a greater occurrence of anticyclonic eddies, though these are weaker than the cyclones observed in other launches. Like summer S2 (east), winter W2 (east) is dominated by stretching regions. The summer S1 (west) distribution shows a somewhat greater occurrence of cyclonic eddies than either S2 or W2 and the indication of frontal areas characterized by increasing α at high ζ. This is consistent with the fact that W1 and S1 both sample the Mississippi River waters, as noted in section 4.2.

Quantification of the structural differences across the launches are given by the probability of occurrence of cyclonic eddies listed in Table 4. The first row $P(\zeta > \alpha, \zeta > 0)$ is simply the probability of finding positive vorticity with relatively smaller strain. Given the significant level of mean cyclonic vorticity in winter W1 (west), nearly half the observations fall into this category. In contrast, the other launches are strain dominated. The conditional probability, $P(\zeta > \alpha | \zeta > 0)$ considers only cyclonic regions. The eddy dominance becomes even clearer for W1 and is increased for the other deployments, although all three remain generally strain-dominated.

Table 4
Probability of Cyclonic Eddies in Each Launch at Scales of 1-km for Winter Launches W1 (West) and W2 (East) and 500-m for Summer Launches S1 (West) and S2 (East)

	W1	W2	S1	S2
$P(\zeta > \alpha, \zeta > 0)$	0.48	0.05	0.17	0.10
$P(\zeta > \alpha \| \zeta > 0)$	0.75	0.15	0.34	0.19

Finally, comparisons of the joint probability distributions of observed vorticty and divergence are shown in Figure 17 for the two winter launches. While there is considerable scatter, even for the data-dense winter launches, the distributions are generally consistent with existing

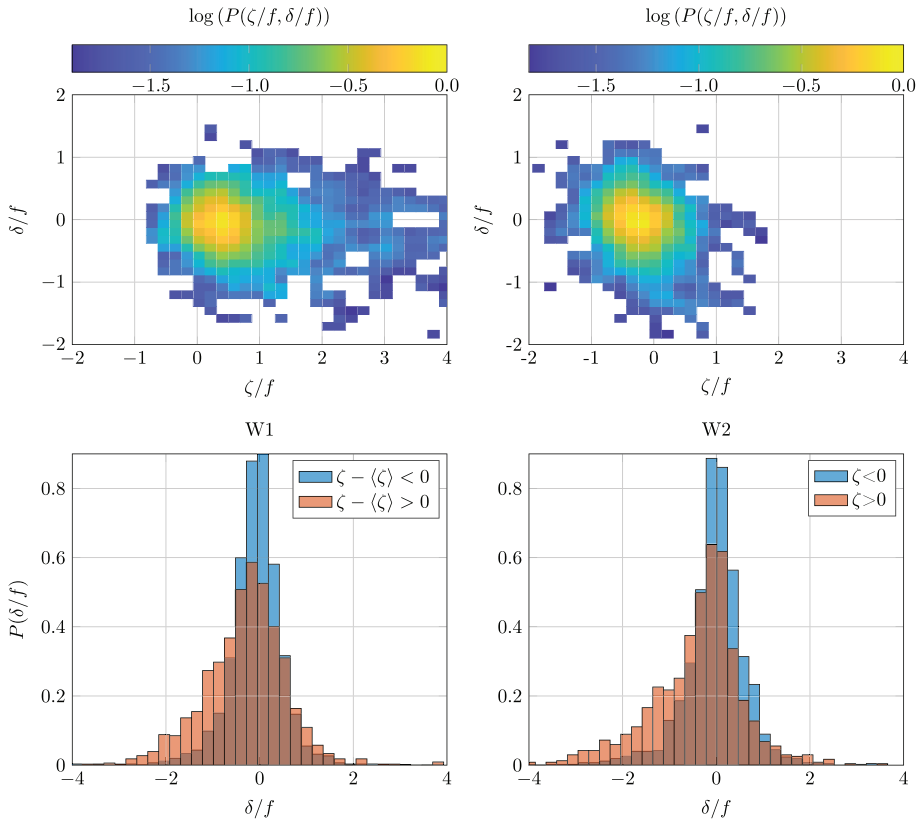

Figure 17. (top panels) Logarithm of the joint distribution of normalized divergence and normalized vorticity in the two winter experiments, W1 (west) and W2 (east). Data are taken from 0.5–2 km triplet scale bins with the distributions normalized by maximum value. (bottom panels) Distributions of scaled divergence conditioned on sign of the observed vorticity.

observational and modeling results (Shcherbina et al., 2013). There is a distinct, but not impenetrable, stability boundary at $Ro = \zeta/f = -1$. As shown in the lower panels, in both experiments, δ/f distributions are nearly symmetric for negative (relative to the mean in W1) vorticity. In contrast, δ/f distributions show strong negative skewness for positive vorticity.

5. Summary and Conclusions

The near-surface submesoscale properties of four different flows in the northern Gulf of Mexico, as observed by extensive, contemporaneous drifter launches, were investigated. The four launches were evenly split between summer and winter seasons, and supporting data allows for the characterization of each launch in terms of atmospheric forcing and vertical density structure of the ocean. The high number of available drifter trajectories permits drifter pair statistics and triplet-based velocity gradient property estimates at horizontal spatial scales ranging from hundreds of meters to several kilometers. In particular, the distribution of vorticity ζ and divergence δ are analyzed across scales. The resulting overall picture reflects both seasonality and spatial inhomogeneities.

Two launches, the winter W1 and the summer S1, took place in the western DeSoto Canyon, in an area influenced by the Mississippi River outflow. Water column stratification in the two launches has obvious differences, with a mixed layer depth of 80 m in winter and 10 m in summer, but in both cases relatively strong small-scale density gradients are present, produced by freshwater filaments of riverine origin. The other two launches occurred in a more eastern location in the DeSoto Canyon, further from the Mississippi River outflow and not directly influenced by it. The winter W2 launch was deployed in an area of laterally homogeneous density, with an 80 m mixed layer, like the other winter deployment and was subjected to strong winds shortly after deployment. The summer S2 launch occurred geographically nearby, but at the

time the area had a 10-m mixed layer like the other summer deployment, was characterized by a strong horizontal salinity gradient, and was subjected to weaker winds.

In each season, one launch targeted a specific flow feature, S2 (east) in summer a persistent density front and W1 (west) in winter a strong cyclone. The specific characteristics of these flows lead to clear differentiations of these two deployments in several metrics. In particular, the S2 deployment—in contrast to the other three—sampled a less ageostrophic flow, with less energy at the submesoscales and dynamics dominated by larger-scale processes, primarily a mesoscale frontal jet. This was reflected in the analysis of two-point structure functions as well as in the scale-dependent kinematic properties, where S2 showed little mean vorticity over all scales and less variance in both vorticity and divergence at scales up to 2 km. These results are consistent with previous analyses by Poje et al. (2014) and Berta et al. (2016), and with the fate of the drifters, caught within a well-defined mesoscale front (Olascoaga et al., 2013). The W1 kinematic property statistics, predictably, are dominated by strong vorticity across all scales. The ζ variance decays at a slower rate with increasing scale than for the other deployments at scales up to 2 km and remains significantly larger at all scales. The velocity gradient discriminant analysis confirms that the flow is heavily eddy dominated.

Winter W2 (east) also exhibits some unique characteristics among the four deployments. Thus, its vorticity distribution does not show the heavy positive tails and high positive skewness observed for the western deployments, winter W1 and summer S1. Also, the flow is mostly dominated by strain rather than vorticity, suggesting that eddy-like structures are rare, with a greater occurrence of anticyclones than cyclones. Overall, the W2 statistics are suggestive of energetic dynamics in the submesoscale range, but do not show the "typical" signature of prevalent high value positive vorticity. This is likely due to the fact that in the absence of horizontal density gradients, typical submesoscale formation mechanisms, such as frontogenesis and mixed layer instabilities that tend to favor positive vorticity, are inhibited. The nature and formation mechanisms of the observed flow need further investigation. A plausible hypothesis is that the strong wind during the measurements plays an important role, either through small-scale forcing inhomogeneity in space or time or through the increase in mixed layer turbulence (D'Asaro, 2014). The range of space scales suggested by our analysis, though, reaches order of 1 km and seems too wide for phenomena such as Langmuir turbulence.

The drifter deployments thus illustrate strong spatial inhomogeneities even within a single season and in the relatively limited area of interest (Figure 1b). Nonetheless, a seasonal signal can also be detected. The summer launches are characterized by reduced energy and kinematic property variances at scales below 3 km. However, the seasonal variability is less pronounced than the variability between different realizations in terms of a number of statistics. This result could be specific to the northern Gulf of Mexico, since the intrusion of the Mississippi freshwater into the saltier and denser Gulf of Mexico water provides a source of surface density gradients also in the summer. This has the potential to significantly impact the submesoscale cycle, possibly introducing a summer secondary maximum as suggested by a modeling study (Luo et al., 2016).

Another novel finding from the results presented here is the remarkable degree of consistency between the scaling of the observed structure functions and the observed scale-dependence of the vorticity and divergence variances, albeit in the realm of log-log power-laws. This suggests that the two-point statistics could provide interesting insights also into three-point metrics.

In summary, the results indicate that the nature of flows in the submesoscale range is complex and variable, depending on both seasons and spatial inhomogeneities. In the presence of mesoscale features, quasi-geostrophic dynamics dominate. Away from mesoscale fronts, the observed flows consistently show relatively high energy at small scales, suggestive of a broad-band wave number spectrum, and strong ageostrophy at scales of the order of 1 km. The additional expected signature of high positive skewness in the vorticity distribution, though, is found only in the launches influenced by the Mississippi River outflow, that guarantees lateral gradients in both seasons. For laterally homogeneous density, this signature is highly reduced or absent. We note that high variability in submesoscale statistics and deviations from the typical signature have been found previously by Ohlmann et al. (2017) in the coastal California Current. The nature of these deviations and the nonubiquity of some of the expected submesoscale properties are still unclear and need to be better understood. Also, the significance of the expected vertical velocity associated with the observed high divergence, its impact in terms of vertical transport of tracers, and its structure need to be further investigated, especially when not associated with the presence of fronts.

Data Availability Statement

All data are publicly available through the Gulf of Mexico Research Initiative Information and Data Cooperative (GRIIDC) at https://data.gulfresearchinitiative.org under the following DOIs: https://doi.org/10.7266/N7VD6WC8 (GLAD drifters), https://doi.org/10.7266/N7ZP441M (GLAD CTD), https://doi.org/10.7266/N7W0940J (LASER drifters), https://doi.org/10.7266/N7H130FC (LASER MVP), and https://doi.org/10.7266/N7N01550 (LASER X-Band Radar).

Acknowledgments
The authors wish to thank the large teams of scientists, technicians, and students that made the GLAD and LASER observational programs possible. This work was supported by grant support from The Gulf of Mexico Research Initiative for the Consortium for Advanced Research on Transport of Hydrocarbon in the Environment (CARTHE) and from the Office of Naval Research under N00014-18-1-2461. The authors are also grateful to two anonymous reviewers whose comments have helped to improve this manuscript.

References

Barkan, R., McWilliams, J. C., Shchepetkin, A. F., Molemaker, M. J., Renault, L., Bracco, A., & Choi, J. (2017). Submesoscale dynamics in the Northern Gulf of Mexico. Part I: Regional and seasonal characterization and the role of river outflow. *Journal of Physical Oceanography*, *47*(9), 2325–2346. https://doi.org/10.1175/JPO-D-17-0035.1

Barkan, R., Molemaker, M. J., Srinivasan, K., McWilliams, J. C., & D'Asaro, E. A. (2019). The role of horizontal divergence in submesoscale frontogenesis. *Journal of Physical Oceanography*, *49*(6), 1593–1618. https://doi.org/10.1175/JPO-D-18-0162.1

Beron-Vera, F. J., & LaCasce, J. H. (2016). Statistics of simulated and observed pair separations in the Gulf of Mexico. *Journal of Physical Oceanography*, *46*(7), 2183–2199. https://doi.org/10.1175/JPO-D-15-0127.1

Berta, M., Griffa, A., Özgökmen, T. M., & Poje, A. C. (2016). Submesoscale evolution of surface drifter triads in the Gulf of Mexico. *Geophysical Research Letters*, *43*, 11,751–11,759. https://doi.org/10.1002/2016GL070357

Boccaletti, G., Ferrari, R., & Fox-Kemper, B. (2007). Mixed layer instabilities and restratification. *Journal of Physical Oceanography*, *37*(9), 2228–2250. https://doi.org/10.1175/JPO3101.1

Buckingham, C. E., Garabato, A. C. N., Thompson, A. F., Brannigan, L., Lazar, A., Marshall, D. P., et al. (2016). Seasonality of submesoscale flows in the ocean surface boundary layer. *Geophysical Research Letters*, *43*, 2118–2126. https://doi.org/10.1002/2016GL068009

Capet, X., McWilliams, J. C., Molemaker, M. J., & Shchepetkin, A. F. (2008a). Mesoscale to submesoscale transition in the California Current system. Part I: Flow structure, eddy flux, and observational tests. *Journal of Physical Oceanography*, *38*(1), 29–43. https://doi.org/10.1175/2007JPO3671.1

Capet, X., McWilliams, J. C., Molemaker, M. J., & Shchepetkin, A. F. (2008b). Mesoscale to submesoscale transition in the California Current system. Part III: Energy balance and flux. *Journal of Physical Oceanography*, *38*(10), 2256–2269. https://doi.org/10.1175/2008JPO3810.1

D'Asaro, E. A. (2014). Turbulence in the upper-ocean mixed layer. *Annual Review of Marine Science*, *6*(1), 101–115. https://doi.org/10.1146/annurev-marine-010213-135138

D'Asaro, E. A., Shcherbina, A. Y., Klymak, J. M., Molemaker, M. J., Novelli, G., Guigand, C. M., et al. (2018). Ocean convergence and the dispersion of flotsam. *Proceedings of the National Academy of Sciences of the United States of America*, *115*(6), 1162–1167. https://doi.org/10.1073/pnas.1718453115

Davis, R. E. (1985). Drifter observations of coastal surface currents during CODE: The statistical and dynamical views. *Journal of Geophysical Research*, *90*(C3), 4756–4772. https://doi.org/10.1029/JC090iC03p04756

Emery, W. J., & Thomson, R. E. (1998). *Data analysis methods in physical oceanography* (pp. 325–327). Amsterdam: Elsevier Science.

Essink, S. (2019). Lagrangian dispersion and deformation in submesoscale flows (Ph.D. Thesis), Massachusetts Institute of Technology.

Fox-Kemper, B., Ferrari, R., & Hallberg, R. (2008). Parameterization of mixed layer eddies. Part I: Theory and diagnosis. *Journal of Physical Oceanography*, *38*(6), 1145–1165. https://doi.org/10.1175/2007JPO3792.1

Frisch, U. (1995). *Turbulence: The legacy of A. N. Kolmogorov*. Cambridge, UK: Cambridge University Press.

Gonçalves, R. C., Iskandarani, M., Özgökmen, T. M., & Thacker, W. C. (2019). Reconstruction of submesoscale velocity field from surface drifters. *Journal of Physical Oceanography*, *49*(4), 941–958. https://doi.org/10.1175/JPO-D-18-0025.1

Haza, A. C., D'Asaro, E., Chang, H., Chen, S. S., Curcic, M., Guigand, C., et al. (2018). Drogue-Loss detection for surface drifters during the Lagrangian Submesoscale Experiment (LASER). *Journal of Atmospheric and Oceanic Technology*, *35*(4), 705–725. https://doi.org/10.1175/jtech-d-17-0143.1

Haza, A. C., Poje, A. C., Özgökmen, T. M., & Martin, P. J. (2008). Relative dispersion from a high-resolution coastal model of the Adriatic Sea. *Ocean Modeling*, *22*(1–2), 48–65. https://doi.org/10.1016/j.ocemod.2008.01.006

Hoskins, B. J. (1982). The mathematical theory of frontogenesis. *Annual Review of Fluid Mechanics*, *14*(1), 131–151. https://doi.org/10.1146/annurev.fl.14.010182.001023

Hua, B. L., & Klein, P. (1998). An exact criterion for the stirring properties of nearly two-dimensional turbulence. *Physica D*, *113*(1), 98–110.

Huang, W., Carrasco, R., Shen, C., Gill, E. W., & Horstmann, J. (2016). Surface current measurements using X-Band marine radar with vertical polarization. *IEEE Transactions on Geoscience and Remote Sensing*, *54*(5), 2988–2997. https://doi.org/10.1109/TGRS.2015.2509781

Huntley, H. S., Lipphardt, B. L. Jr., & Kirwan, A. D. Jr. (2019). Anisotropy and inhomogeneity in drifter dispersion. *Journal of Geophysical Research: Oceans*, *124*, 8667–8682. https://doi.org/10.1029/2019JC015179

Karimova, S., & Gade, M. (2016). Improved statistics of sub-mesoscale eddies in the Baltic Sea retrieved from SAR imagery. *International Journal of Remote Sensing*, *37*(10), 2394–2414. https://doi.org/10.1080/01431161.2016.1145367

Kawai, H. (1985a). Scale dependence of divergence and vorticity of near-surface flows in the sea. Part 1. Measurements and calculations of area-averaged divergence and vorticity. *Journal of the Oceanographical Society of Japan*, *41*(3), 157–166. https://doi.org/10.1007/BF02109190

Kawai, H. (1985b). Scale dependence of divergence and vorticity of near-surface flows in the sea. Part 2. Results and interpretation. *Journal of the Oceanographical Society of Japan*, *41*(3), 167–175. https://doi.org/10.1007/BF02111116

Kirwan, A. D. Jr. (1988). Notes on the cluster method for interpreting relative motions. *Journal of Geophysical Research*, *93*(C8), 9337–9339. https://doi.org/10.1029/JC093iC08p09337

Klein, P., Lapeyre, G., Siegelman, L., Qiu, B., Fu, L.-L., Torres, H., et al. (2019). Ocean-scale interactions from space. *Earth and Space Science*, *6*, 795–817. https://doi.org/10.1029/2018EA000492

Klymak, J. M., Shearman, R. K., Gula, J., Lee, C. M., D'Asaro, E. A., Thomas, L. N., et al. (2016). Submesoscale streamers exchange water on the north wall of the Gulf Stream. *Geophysical Research Letters*, *43*, 1226–1233. https://doi.org/10.1002/2015GL067152

Kolmogorov, A. N. (1941). Dissipation of energy in locally isotropic turbulence. In *Proceedings of the USSR Academy of Sciences* (Vol. 32, pp. 16). Moskva, Russian Federation: Akademiia nauk SSSR. [Reprinted in Proceedings of the Royal Society of London, A, 434, 9-13, (1991).]

LaCasce, J. H. (2008). Statistics from Lagrangian observations. *Progress in Oceanography*, *77*(1), 1–29. https://doi.org/10.1016/j.pocean.2008.02.002

LaCasce, J. H., & Ohlmann, J. C. (2003). Relative dispersion at the surface of the Gulf of Mexico. *Journal of Marine Research*, *61*(3), 285–312. https://doi.org/10.1357/002224003322201205

Lévy, M., Franks, P. J. S., & Smith, K. S. (2018). The role of submesoscale currents in structuring marine ecosystems. *Nature Communications*, *9*(1), 4758–16. https://doi.org/10.1038/s41467-018-07059-3

Lund, B., Haus, B. K., Horstmann, J., Graber, H. C., Carrasco, R., Laxague, N. J. M., et al. (2018). Near-surface current mapping by shipboard marine X-band radar: A validation. *Journal of Atmospheric and Oceanic Technology*, *35*(5), 1077–1090. https://doi.org/10.1175/JTECH-D-17-0154.1

Luo, H., Bracco, A., Cardona, Y., & McWilliams, J. C. (2016). Submesoscale circulation in the northern Gulf of Mexico: Surface processes and the impact of the freshwater river input. *Ocean Modelling*, *101*, 68–82. https://doi.org/10.1016/j.ocemod.2016.03.003

Mahadevan, A., & Tandon, A. (2006). An analysis of mechanisms for submesoscale vertical motion at ocean fronts. *Ocean Modelling*, *14*(3–4), 241–256. https://doi.org/10.1016/j.ocemod.2006.05.006

McWilliams, J. C. (2016). Submesoscale currents in the ocean. *Proceedings of the Royal Society A*, *472*, 20160117. https://doi.org/10.1098/rspa.2016.0117

Mensa, J. A., Garraffo, Z. D., Griffa, A., Özgökmen, T. M., Haza, A. C., & Veneziani, M. (2013). Seasonality of the submesoscale dynamics in the Gulf Stream region. *Ocean Dynamics*, *63*(8), 923–941. https://doi.org/10.1007/s10236-013-0633-1

Molinari, R., & Kirwan, A. D. Jr. (1975). Calculations of differential kinematic properties from Lagrangian observations in the Western Caribbean Sea. *Journal of Physical Oceanography*, *5*(3), 483–491. https://doi.org/10.1175/1520-0485(1975)005<0483:CODKPF>2.0.CO;2

Munk, W., Armi, L., Fischer, K., & Zachariasen, F. (2000). Spirals on the sea. *Proceedings of the Royal Society A*, *456*(1997), 1217–1280. https://doi.org/10.1098/rspa.2000.0560

Novelli, G., Guigand, C. M., Cousin, C., Ryan, E. H., Laxague, N. J. M., Dai, H., et al. (2017). A biodegradable surface drifter for ocean sampling on a massive scale. *Journal of Atmospheric and Oceanic Technology*, *34*(11), 2509–2532. https://doi.org/10.1175/JTECH-D-17-0055.1

Ohlmann, J. C., Molemaker, M. J., Baschek, B., Holt, B., Marmorino, G., & Smith, G. (2017). Drifter observations of submesoscale flow kinematics in the coastal ocean. *Geophysical Research Letters*, *44*, 330–337. https://doi.org/10.1002/2016GL071537

Okubo, A. (1970). Horizontal dispersion of floatable particles in the vicinity of velocity singularities such as convergences. *Deep Sea Research*, *17*(3), 445–454. https://doi.org/10.1016/0011-7471(70)90059-8

Okubo, A., Ebbesmeyer, C. C., & Helseth, J. M. (1976). Determination of Lagrangian deformations from analysis of current followers. *Journal of Physical Oceanography*, *6*(4), 524–527. https://doi.org/10.1175/1520-0485(1976)006<0524:DOLDFA>2.0.CO;2

Olascoaga, M. J., Beron-Vera, F. J., Haller, G., Triñanes, J., Iskandarani, M., Coelho, E. F., et al. (2013). Drifter motion in the Gulf of Mexico constrained by altimetric Lagrangian coherent structures. *Geophysical Research Letters*, *40*, 6171–6175. https://doi.org/10.1002/2013GL058624

Özgökmen, T. M., & Fischer, P. F. (2012). CFD application to oceanic mixed layer sampling with Lagrangian platforms. *International Journal of Computational Fluid Dynamics*, *26*(6–8), 337–348. https://doi.org/10.1080/10618562.2012.668888

Poje, A. C., Özgökmen, T. M., Bogucki, D. J., & Kirwan, A. D. Jr. (2017). Evidence of a forward energy cascade and Kolmogorov self-similarity in submesoscale ocean surface drifter observations. *Physics of Fluids*, *29*(2), 020701. https://doi.org/10.1063/1.4974331

Poje, A. C., Özgökmen, T. M., Lipphardt, B. L. Jr., Haus, B. K., Ryan, E. H., Haza, A. C., et al. (2014). Submesoscale dispersion in the vicinity of the *deepwater horizon* spill. *Proceedings of the National Academy of Sciences of the United States of America*, *111*(35), 12,693–12,698. https://doi.org/10.1073/pnas.1402452111

Rudnick, D. L. (2001). On the skewness of vorticity in the upper ocean. *Geophysical Research Letters*, *28*(10), 2045–2048. https://doi.org/10.1029/2000GL012265

Sasaki, H., Klein, P., Qiu, B., & Sasai, Y. (2014). Impact of oceanic-scale interactions on the seasonal modulation of ocean dynamics by the atmosphere. *Nature Communications*, *5*(1), 5636. https://doi.org/10.1038/ncomms6636

Senet, C. M., Seemann, J., & Ziemer, F. (2001). The near-surface current velocity determined from image sequences of the sea surface. *IEEE Transaction on Geoscience and Remote Sensing*, *39*(3), 492–505. https://doi.org/10.1109/36.911108

Shcherbina, A. Y., D'Asaro, E. A., Lee, C. M., Klymak, J. M., Molemaker, M. J., & McWilliams, J. C. (2013). Statistics of vertical vorticity, divergence, and strain in a developed submesoscale turbulence field. *Geophysical Research Letters*, *40*, 4706–4711. https://doi.org/10.1002/grl.50919

Shulman, I., Penta, B., Richman, J., Jacobs, G. A., Anderson, S., & Sakalaukus, P. (2015). Impact of submesoscale processes on dynamics of phytoplankton filaments. *Journal of Geophysical Research: Oceans*, *120*, 2050–2062. https://doi.org/10.1002/2014JC010326

Thomas, L. N., & Lee, C. M. (2005). Intensification of ocean fronts by down-front winds. *Journal of Physical Oceanography*, *35*(6), 1086–1102. https://doi.org/10.1175/JPO2737.1

Weiss, J. (1991). The dynamics of enstrophy transfer in two-dimensional hydrodynamics. *Physica D*, *48*(2–3), 273–294. https://doi.org/10.1016/0167-2789(91)90088-Q

Yaremchuk, M., & Coelho, E. F. (2015). Filtering drifter trajectories sampled at submesoscale resolution. *IEEE Journal of Oceanic Engineering*, *40*(3), 497–505. https://doi.org/10.1109/JOE.2014.2353472